Novel synthesis method of BaTiO$_3$-nanoparticles

Synthesis of BaTiO$_3$-nanoparticles by
spray-pyrolysis of TiO$_2$-nanoparticles
dispersed in Ba(NO$_3$)$_2$-solution

Magnus Gryteselv

Preface

This thesis is submitted to the Norwegian University of Science and Technology (NTNU). It is part of the requirements for the degree of Master of Science in the study program Industrial chemistry and Biotechnology. The work was carried out from January to June 2016. The work was done partly in cooperation with CerPoTech AS, who supplied the precursor materials and carried out the spray pyrolysis of the suspensions. Professor Mari-Ann Einarsrud at the Department for Materials Science and Engineering at NTNU was the main supervisor of this work, with post doctorate fellow Julia Glaum at NTNU and Dr. Sophie Labonnote-Weber at CerPoTech AS serving as co-supervisors.

I would like to thank my supervisors for all the help, discussions and feedback they have provided during the semester. I need to thank Julia Glaum in particular, for proof-reading this thesis. I would also like to thank all of my co-workers in the Ferroics group and the technical staff at the Department of Materials Science and Engineering at NTNU. A thank you to Sigrid Sognli Høyem is also in order, for mutual sharing of articles, discussions, and long coffee breaks.

All laboratory work was done by Magnus Gryteselv, with the exception of preparation of the BTO-a solution and the spray pyrolysis of the suspensions. This thesis is a continuation of the specialization project[1] by the author carried out from August to December 2015. The most relevant experimental work and results from the specialization project are included in this thesis to give a more complete understanding of the entire process. The parts included from the specialization project are the production of the first BTO-c and BTO-n suspensions, the spray-pyrolysis of the suspensions, and powder characterization by SEM and XRD.

23.06.2016

Magnus Gryteselv

Abstract

Ferroelectric materials are widely used in different technological applications today. Lead zirconate titanate (PZT) materials are currently the most used, due to their excellent piezoelectric properties and relatively high operating temperatures. However, due to high lead content and its environmental toxicity, lead-free alternatives are being explored. One such material is barium titanate ($BaTiO_3$). Finding cheap, energy-efficient, and scalable synthesis methods for such materials is necessary to start phasing out PZT in favor of more environmentally friendly alternatives.

The particle size of ceramic powders is an important property as many materials exhibit different physical behavior when the particle size is in the nanometer range. Increased material strength, unique optical properties, and increased reactivity are some examples. Several applications of ceramic powders rely on this phenomenon; e.g. increased sintering activity where fine powder is needed to promote densification.

This work explores the possibility of synthesizing $BaTiO_3$-nanoparticles through spray pyrolysis of a suspension with TiO_2-nanoparticles dispersed in a barium nitrate solution. $BaTiO_3$-nanoparticles with particle size between 50-100 nm were achieved. The importance of suspension stability with regard to phase purity and yield of produced powder was investigated. The results of the powder characterization indicate that complexing the barium-ions with ethylenediaminetetraacetic acid (EDTA) and citric acid (CA) may be necessary to achieve satisfactory stability and stoichiometric control of the suspension. Pellets were produced and the sintering behavior and piezoelectric properties of these pellets were investigated. The piezoelectric properties of the samples are comparable to reported values for $BaTiO_3$ in regards to polarization values, but significantly lower than reported in regards to measured displacement values.[2][3] The results indicate some contamination or secondary phase formation in the samples. The contamination is believed to originate from either the precursor powders, the spray-pyrolysis equipment or process, or a combination of both.

Further work is required to determine the usefulness of the method. The suspension stability must be improved to ensure stoichiometric control during the process. The source of the contamination or secondary phase formation must also be identified and eliminated.

Sammendrag

Ferroelektriske materialer har i dag mange bruksområder i forskjellige teknologiske applikasjoner. Blyzirkonattitanat (PZT) er den gruppen av materialer som for øyeblikket er mest brukt, på grunn av gode piezoelektriske egenskaper og relativt høye brukstemperaturer. Blyfrie alternativer undersøkes imidlertid i stadig større grad, da PZT inneholder relativt store mengder miljøskadelig bly. Et slikt blyfritt materiale er bariumtitanat ($BaTiO_3$). For at PZT skal kunne fases ut er det nødvendig å finne billige, energieffektive og skalerbare metoder for å produsere blyfrie alternativer som $BaTiO_3$.

Partikkelstørrelsen I keramiske pulvere er en viktig parameter da mange materialer får andre fysiske egenskaper når partikkelstørrelsen er i nanometer-området, for eksempel økt materialstyrke, unike optiske egenskaper og økt reaktivitet. Mange bruksområder for keramiske materialer er avhengig av denne egenskapen, for eksempel keramiske nanopulverkatalysatorer.

Denne rapporten utforsker mulighetene for syntetisering av $BaTiO_3$-nanopartikler gjennom spraypyrolyse av en suspensjon med anatase TiO_2-nanopartikler dispergert i en bariumnitratløsning. Det ble syntetisert $BaTiO_3$ med partikkelstørrelse mellom 50-100 nm. Viktigheten av stabile suspensjoner med tanke på faserenhet og utbytte av syntesemetoden ble demonstrert. Resultatene indikerer at kompleksering av bariumionene i suspensjonene kan være nødvendig for å oppnå tilfredsstillende stabile suspensjoner og støkiometrisk kontroll. De produserte pulverne ble presset til pellets og sintringsegenskapene og de piezoelektriske egenskapene ble undersøkt. De piezoelektriske egenskapene til prøvene stemmer godt overens med litteraturverdier når det gjelder polariasjonsverdier, men er lavere enn rapporterte tøyningsverdier.[2] [3] Resultatene indikerer noe kontaminering eller formasjon av sekundære faser i prøvene. Kilden til kontamineringen eller sekundærfasene er antatt å stamme fra utgangsstoffene, spray-pyrolyseprosessen, eller en kombinasjon av disse.

Videre arbeid er nødvendig for å bestemme brukbarheten til denne metoden. Suspensjonsstabiliteten må forbedres for å sikre støkiometrisk kontroll i løpet av prosessen. Kilden til kontamineringen eller sekundærfaseformasjonen må også identifiseres og elimineres fra prosessen.

Contents

1 Background

1.1 Motivation

Pierre and Jacques Curie first reported the piezoelectric effect in 1880. They demonstrated the effect in natural and laboratory grown single crystals of quartz, tourmaline, cane sugar, topaz, and Rochelle salt.[4] Ferroelectricity was first reported over 40 years later, in 1921. The ferroelectric effect was first discovered in Rochelle salt single crystals, and then in polycrystalline $BaTiO_3$ in the early 1940's.

Since the discovery of the ferroelectric effect, a continuous development of new materials has led to a wide variety of applications of ferroelectrics.[5] Ferroelectric materials are key components in transformers, sensors, and actuators.

PZT is the most commonly used material for piezoelectric applications today. However, a significant effort is being put into discovering new materials with comparable properties to replace PZT, due to regulations for use of lead in electronics issued by the European Union.[6] These regulations are set in place due to the environmental toxicity of lead. As there currently are no realistic alternatives to PZT, an exception has been made for devices that rely on PZT until an alternative is found.[6]

Several methods exist for synthesis of powders of ferroelectric materials. One such method is spray-pyrolysis of precursor solutions. This is an effective, fast, and scalable method, and by using water-soluble precursors, the amount of organic waste is reduced. Spray-pyrolysis results in powders with small particle size, and this is an important parameter for the application of ferroelectric materials. When using solutions or stable suspensions, this method gives good control of stoichiometry and allows for production of tailored element compositions.

1.2 Aim of work

The aim of this work was to explore the possibilities for production of $BaTiO_3$ powders by spray-pyrolysis of TiO_2-nanoparticles suspended in a barium nitrate solution. The powder was characterized, and the piezoelectric properties tested to compare the synthesized powder to commercially available powders. Comparable properties would mean that spray pyrolysis with suspensions as a precursor could provide an easy and cheap alternative synthesis route for $BaTiO_3$ powder. It also has the added benefit of avoiding the use of solutions of organic titanium salts. Organic titanium salts are both more expensive than TiO_2, and harder to work with, as they often require very acidic conditions to dissolve in water. TiO_2 is a practically inert, non-toxic and very cheap compound, which makes it favorable as a source of titanium over organic titanium salts, e.g. titanium isopropoxide.

Important properties of the produced powder include phase purity, small particle size and homogenous particle size distribution. The effect of suspension composition, suspension stability, and calcining parameters on the phase purity and particle size of the synthesized powder, as well as the piezoelectric properties of sintered samples, was investigated. The results were compared to $BaTiO_3$ produced by spray pyrolysis of a barium nitrate-titanium isopropoxide solution. The properties of the produced powders will give an indication of the applicability of spray pyrolysis of suspensions as a synthesis method to produce $BaTiO_3$.

2 Introduction

The basic concepts of piezoelectricity and common piezoelectric materials are explained in section 2.1. Dispersion theory and suspension behavior are explained in section 2.2 to give the necessary background for the methods used in this work. Ceramic powder synthesis methods, characterization of ceramic powders, and pressing and sintering behavior are discussed in sections 2.3-2.6.

2.1 Piezoelectricity

Piezoelectricity is a phenomenon connecting the application of mechanical stress to a material with a change in its polarization state. Direct piezoelectricity is change in polarization in single crystals or unit cells in dielectric materials when stress is applied. Such crystals or unit cells will, when affected by an applied stress, gain a net positive charge on one side and a net negative charge on the other side resulting in a measurable electrical potential, illustrated in Figure 2.1. The converse piezoelectric effect is in turn when application of an external electric field induces mechanical deformation of the crystal. Piezoelectricity is thus a phenomenon that connects mechanical and electrical energy. For a material to be able to exhibit piezoelectric properties, it must be anisotropic and the crystals must not have a center of symmetry.[4]

The relation between dielectric displacement, D (Charge Q per unit area A), and the stress T in the direct piezoelectric effect can be written as:

$$D = \frac{Q}{A} = d_{ij}T$$

The piezoelectric constant d_{ij} is in Coulombs per Newton, and is directional. d_{33} is the constant in the direction of the polarization. In the converse piezoelectric effect, the relation between the electric field, E, and the strain, S, can be written as:

$$S = d_{ij}E$$

Here, d_{ij} is given in meters per Volt. The piezoelectric constant d_{ij} is numerically identical for the direct and converse effect. If the two equations for the piezoelectric effect are rearranged, the piezoelectric constant can be written as:

$$d_{ij} = \frac{S}{E} = \frac{D}{T}$$

When rearranged this way, it can be seen that a high value for d_{ij} means that the material has a high response; A small change in stress and strain leads to large changes in dielectric displacement and electric field respectively.[7]
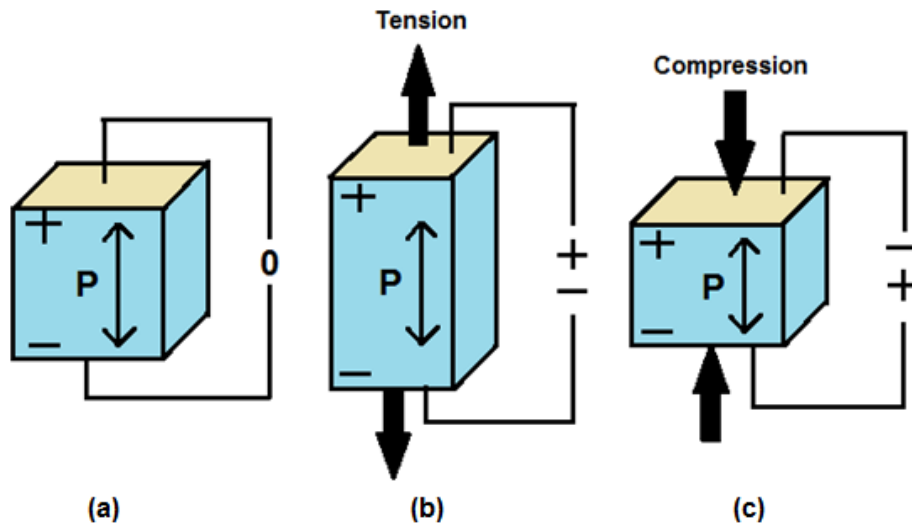
Figure 2.1: Illustration of the piezoelectric effect during tension (b) and compression (c).[8]

Pyroelectric materials are a sub-class of piezoelectric materials, as illustrated in Figure 2.2. This class of materials develops spontaneous polarization if cooled below the Curie temperature. The degree of polarization in a pyroelectric material changes when the material is heated due to the mechanical deformation induced by thermal expansion.
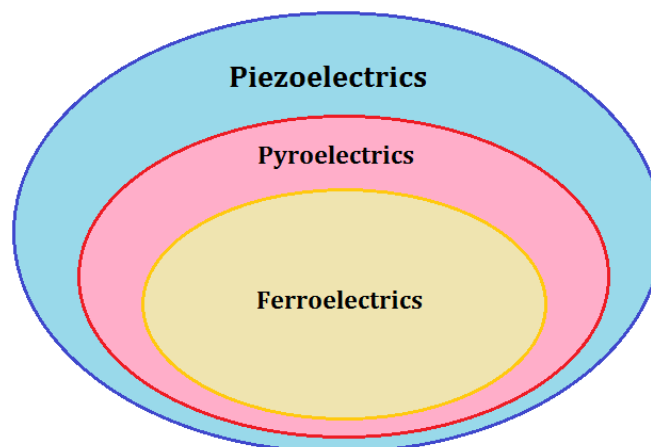
Figure 2.2: Relationship between piezoelectricity, pyroelectricity and ferroelectricity.[1]

The Curie temperature is an important property of pyro- and ferroelectric materials. It is named after Pierre Curie, who discovered that above a critical temperature, certain materials lost their permanent magnetic properties. For a ferroelectric material, the Curie temperature is the temperature limit where upon heating, a phase transition from a ferroelectric phase to a non-ferroelectric phase occurs[9].

2.1.1 Ferroelectricity

Ferroelectric materials are a sub-class of pyroelectric materials, as illustrated in Figure 2.2. They have the same properties as pyroelectric materials, with a few key additions. As with pyroelectric materials, ferroelectric materials have a spontaneous polarization. For a material to be able to have ferroelectric properties, the crystal must contain alternate stable atom positions or molecular orientations so the dipole can be reversed. However, the direction of polarization can be reversed by application of an electric field, and the resulting polarization-electric field curve follows a hysteresis loop. This enables the material to keep its polarization even after the applied voltage is removed.[4]

An example of a ferroelectric hysteresis loop can be seen in Figure 2.3. As the electric field, E, increases, the polarization increases along the lower line in the diagram. As the field is gradually reversed, the polarization decreases and changes direction along the upper line in the diagram. When the field reaches zero after having reached maximum field, the remnant polarization can be measured. This is the polarization that is retained in the structure even after the field is removed. The change in polarization is slow near the maximum polarization values, and abrupt further away. This is because displacement of the central atom in one of the two directions is the most stable state when the temperature of the material is below the Curie temperature. Also shown in Figure 2.3 is the strain-electric field curve of a typical ferroelectric material.
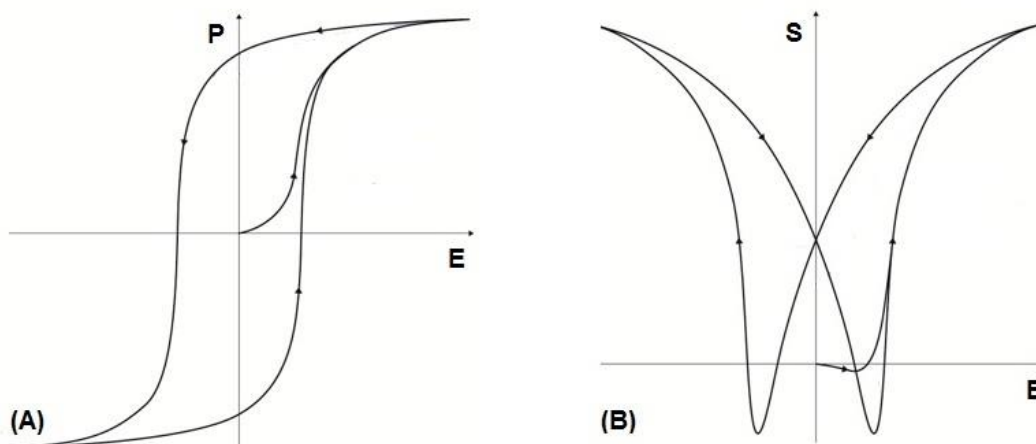

Figure 2.3: The polarization-field curve (A), and the strain-field curve of a typical ferroelectric material (B).[10]

For polycrystalline ferroelectric material, areas with different direction of spontaneous polarization will exist within the structure. An area where all atoms are aligned with the same polarization direction ia called a ferroelectric domain. Domains will, when subjected to a strong enough electric field, align parallel to the direction of the electric field. Domains that are switched 90° in relation to the original polarization direction will require a stronger field to switch than domains that are switched 180°, because more strain will be induced in the material.

2.1.2 Ferroelectric materials

Out of the 32 crystal point groups, 20 of them are piezoelectric. 10 of the 20 piezoelectric point groups are pyroelectric, and some of those 10 are ferroelectric.[5] The ABO_3 perovskites are typical ferroelectric materials. A and B are often alkaline or rare-earth elements or metals (e.g. Sr, Bi, and Ba) and transition metals (e.g. Ti, Fe, and Mn) respectively, i.e. $SrTiO_3$, $BiFeO_3$ and $LaYbO_3$. Figure 2.4 shows the unit cell of an ABO_3 perovskite. Common uses for ferroelectrics are in transducers, capacitors, actuators and pressure or heat sensors.[5]
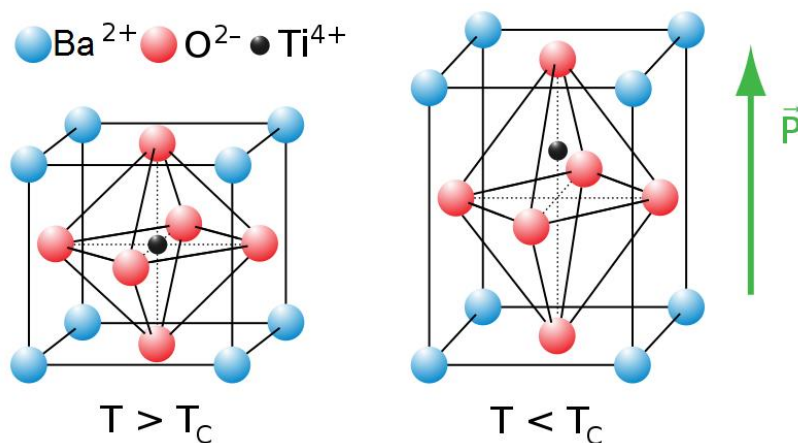
Figure 2.4: Illustration of the perovskite structure in $BaTiO_3$ and PZT. In PZT, the Ba^{2+}-atoms are replaced with Pb^{2+}, and some central Ti^{4+}-ions are replaced with Zr^{4+}. The figure shows the spontaneous polarization that occurs when the material is below the Curie-temperature because of displacement of Ti^{4+}.[11]

The most widely used ferroelectric materials today are different variants of lead zirconate titanate, abbreviated PZT. They are among the most versatile ferroelectric materials, due to their high coupling constants and wide variety of possible stoichiometries. PZT-materials have a high sensitivity, meaning they have a large piezoelectric response from induced deformation[12], and relatively high operating temperature. Some PZT variants can have Curie temperatures as high as 350 °C.[13] However, due to a lead-content of around 60 wt. percent and the environmental toxicity associated with lead, lead-free alternatives are in high demand.[14]

BaTiO₃

One lead-free alternative to PZT is barium titanate, or $BaTiO_3$. $BaTiO_3$ was the first perovskite material with ferroelectric properties to be discovered. One of the first applications of $BaTiO_3$ was in capacitors, due to the high dielectric constant of the material.[5] The unit cell of $BaTiO_3$ is shown in Figure 2.4. Above the Curie temperature, $BaTiO_3$ is cubic and does not show spontaneous polarization, and thus no ferroelectric properties. Below the Curie temperature, $BaTiO_3$ takes on the tetragonal *P4mm* structure, and gains ferroelectric properties due to displacement of the central Ti^{4+}, see Figure 2.4. The temperature-pressure phase diagram of $BaTiO_3$ is shown in Figure 2.5.
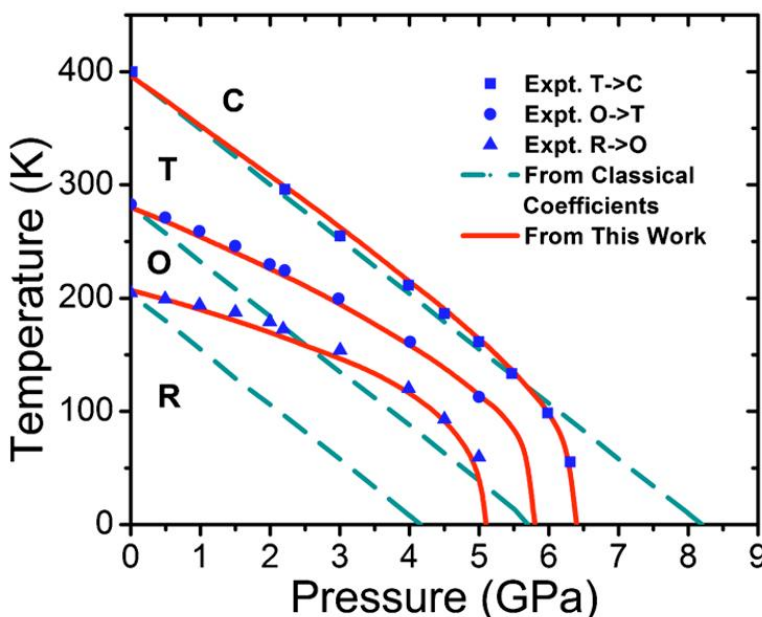
Figure 2.5: Temperature-pressure phase diagram of $BaTiO_3$. The blue squares, circles and triangles marks the experimental tetragonal-cubic, orthorhombic-tetragonal, and the rhombohedral-orthorhombic phase boundaries respectively. The red lines are theoretical approximations of the same phase boundaries derived by Wang et. Al. The green dashed lines are the classical theoretical phase boundaries where a simple pressure-dependency is assumed. This figure is from the work of Wang et. Al. [15]

At ambient pressure, the maximum temperature for applications of $BaTiO_3$ that utilize its ferroelectric properties is around 120 °C (393 K). This is due to the transformation from ferroelectric tetragonal $BaTiO_3$ to non-ferroelectric cubic $BaTiO_3$, illustrated in the temperature-pressure diagram in Figure 2.5. The orthorhombic-tetragonal phase transition is also problematic, as it occurs close to room temperature, at around 5 °C (278 K). This change in structure has several implications for the application of $BaTiO_3$, as the ferroelectric properties change with the structure. The phase transition temperatures can be influenced by doping. Common dopants in $BaTiO_3$ include calcium[16], zirconium, lanthanum, and strontium.[17]

The BaO-TiO_2 binary phase diagram can be seen in Figure 2.6. It shows that several phases of barium titanate are stable. The most important ones for this work are $BaTiO_3$ as well as Ba_2TiO_4, which forms for excess of Ba^{2+}, and $BaTi_2O_5$, which forms for excess of Ti^{4+}. It should also be noted that above 1320 °C, liquid phase formation occurs.
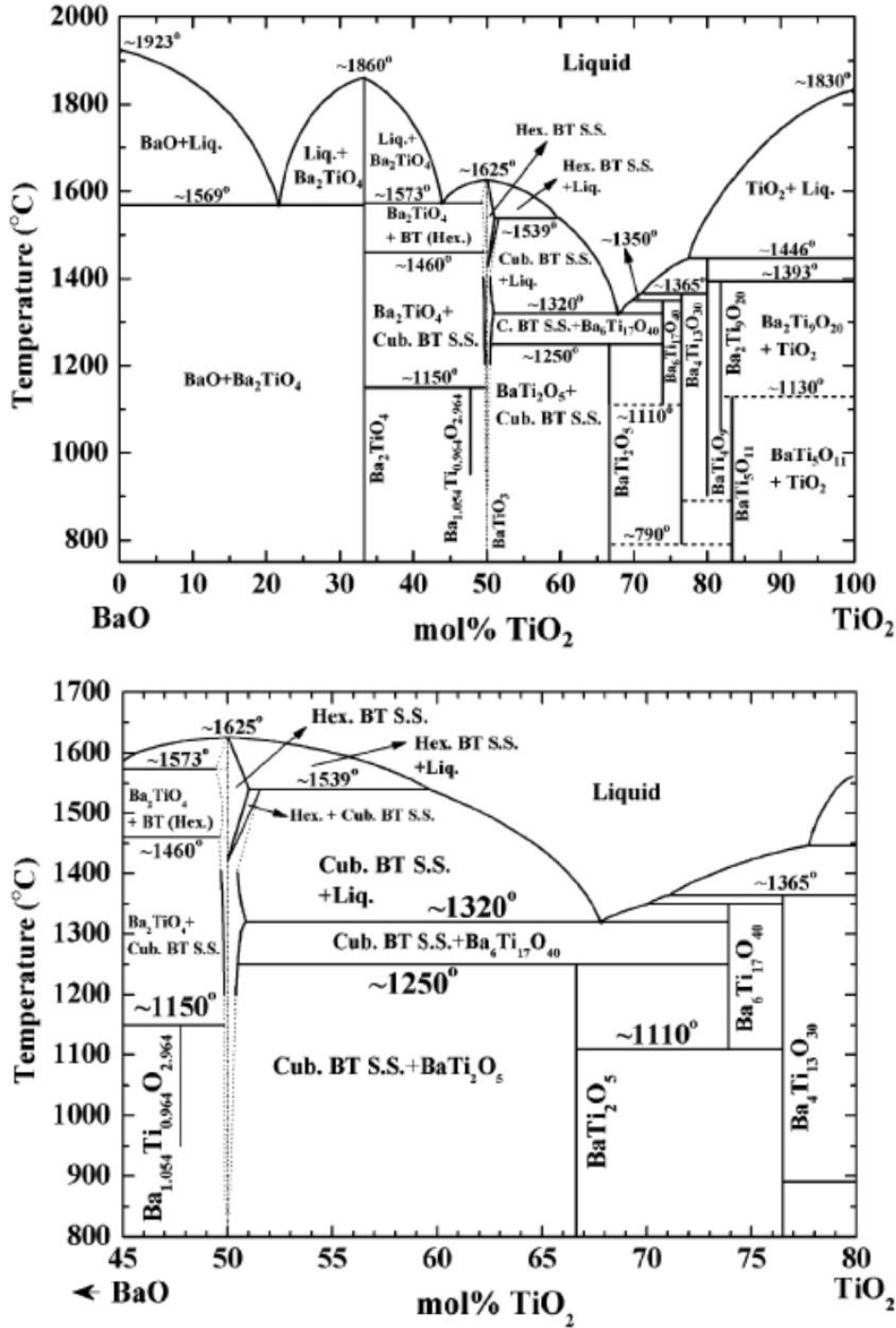

Figure 2.6: Binary phase-diagram of the BaO-TiO_2 system. $BaTiO_3$ forms at stoichiometric amounts of Ba^{2+} and Ti^{4+}. For a ratio of concentration of Ti^{4+}/Ba^{2+} less than 1, Ba_2TiO_4 may form.[18]

2.2 Dispersion stability

In order to produce high-quality powders using a spray-pyrolysis process, the stabilities of the precursor suspensions are important. Spraying of non-stable suspensions may lead to sedimentation, which causes loss of control of reaction stoichiometry and poor reaction yield. Sedimentation of dispersed particles may cause loss of reactants during the spray pyrolysis process as not all of the powder enters the furnace. The dispersion stability of particles in a liquid solvent depend on several parameters, the most important of which are discussed in this section.

To explain the interactions between particles dispersed in a liquid media, the DLVO theory is commonly used. It is named after Derjaguin, Landau, Verwey and Overbeek, and was first proposed by Derjaguin and Landau in 1941. Seven years later, Verwey and Overbeek independently obtained the same results. The DLVO theory combines the effects of attractive Van der Waals forces and repulsive double layer forces to explain the stability, or lack thereof, of colloidal suspensions.[19]

2.2.1 Van der Waals attractive forces

Van der Waals forces are intermolecular forces between permanent or induced dipoles. The magnitude of these forces depend heavily on the distance between the molecules, and is reduced with increasing intermolecular distance, as shown in Figure 2.7.
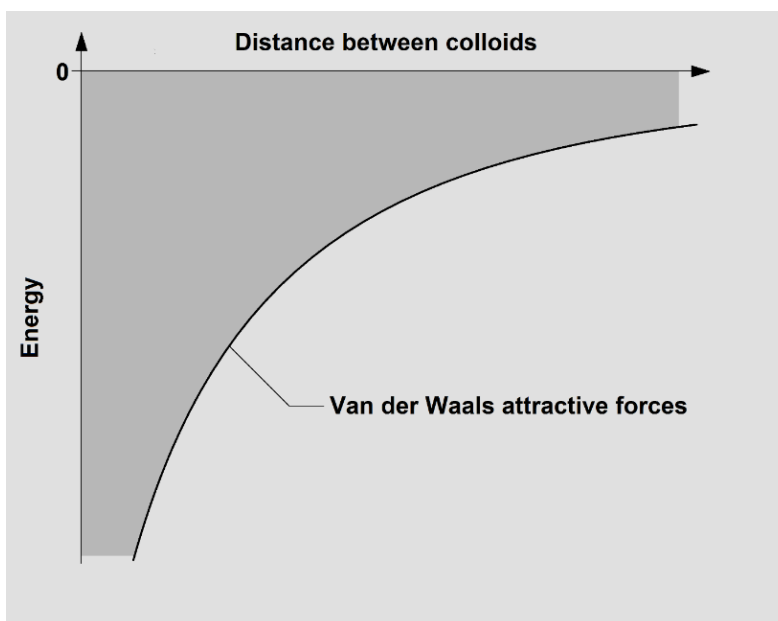

Figure 2.7: The curve shows how the energy between two particles due to Van der Waals attractive forces change depending on the distance between the particles.

This relationship can be described by the Derjaguin approximation:

$$W(D) = -\frac{A}{6D} \cdot \frac{R_1 R_2}{R_1 + R_2}$$

where $W(D)$ is the free energy between two particles 1 and 2, D is the distance between them, A is the Hamaker constant, and R_1 and R_2 are the radii of the two particles. In most cases, the Hamaker constant is positive. The Van der Waals forces are therefore usually attractive. Attractive forces are often defined as negative energy between particles, and repulsive forces are defined as positive energy between particles, a definition also used in this work.

2.2.2 Double layer repulsive forces

The double layer is a visualization of the ionic environment around a charged particle. This model is used to explain the repulsive electrical forces that are observed around charged particles. For a negatively charged particle, positive ions are drawn to its surface where they create a thin, dense layer known as the Stern layer. The positive ions are considered to be firmly bound to the surface of the negative particle. Outside of this layer, additional positive ions that are attracted to the negatively charged particle, will be repelled by the positive ions in the Stern layer. This is called the diffuse layer. Together, these two layers make up the double layer. Figure 2.8 is a visualization of the double layer around a negatively charged ion.
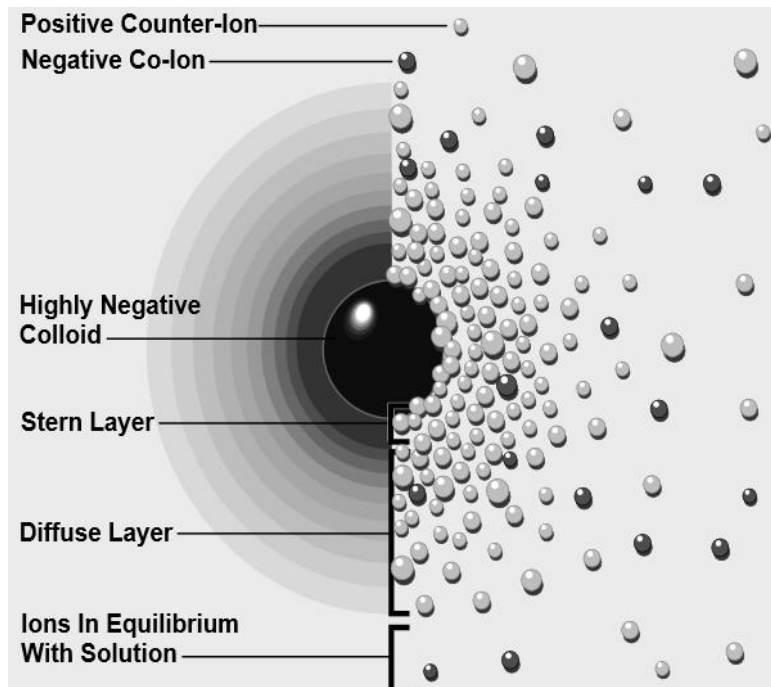

Figure 2.8: Illustration of how the ionic environment near a negative colloidal particle is imagined in the double layer theory.[20]

The double layer formation will result in a net repulsive electrical force near the surface of the negative particle. The magnitude of this force is reducing with increasing distance from the particle, as illustrated in Figure 2.9.
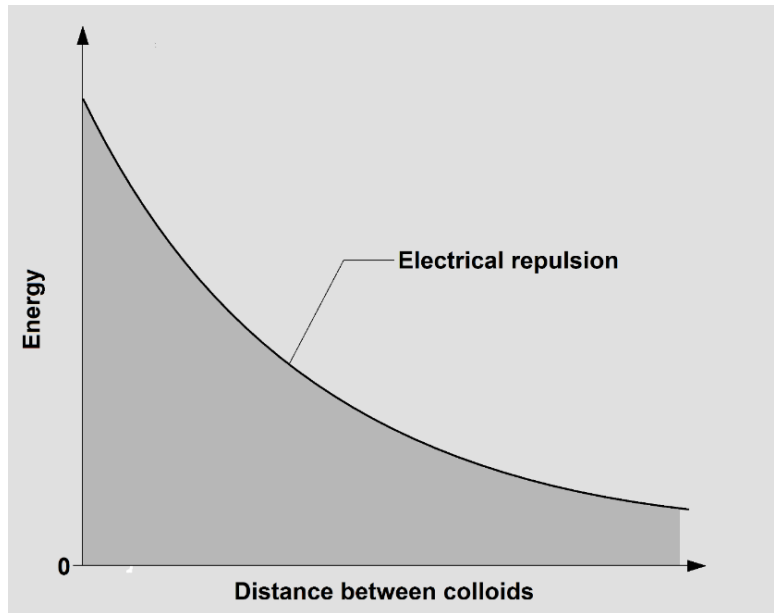
Figure 2.9: The curve shows how the energy between to particles due to double layer repulsive forces change depending on the distance between the particles.

When the double layer is formed, it results in an electrokinetic potential difference between the surface of the particle and the surrounding liquid. This potential is strongest at the surface of the particle, and reduces with increasing distance from the surface. At the surface, it is called surface potential.

The Zeta potential is defined as the potential at the boundary between the Stern layer and the diffuse layer, as shown in Figure 2.10. The Stern layer is considered tightly bound to the particle, while the diffuse layer is loosely bound. The Zeta potential is related to the mobility of a charged particle in a liquid, as the mobility depends on the potential between a particle and the surrounding liquid. The other parameters that affect the particle mobility are the dielectric constant of the particle material, and the viscosity of the liquid.

When the charge of the negatively charged particle is fully balanced by positive ions in the surrounding environment, it is called the point of zero charge, or p.z.c. for short.
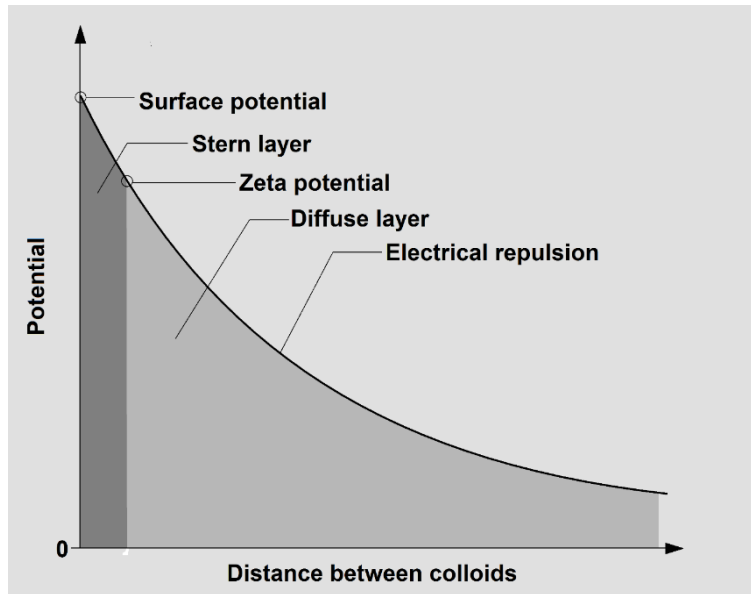
Figure 2.10: The curve shows how the surface potential and the Zeta potential are defined. The dark area in the figure represents the Stern layer, while the lighter area represents the diffuse layer.

2.2.3 Combined effect

The net interaction energy between colloids or particles can be obtained by adding together the contributions from the attractive Van der Waals forces and the repulsive double layer forces. In Figure 2.11, the contribution from both forces are combined, illustrating the net interaction energy.
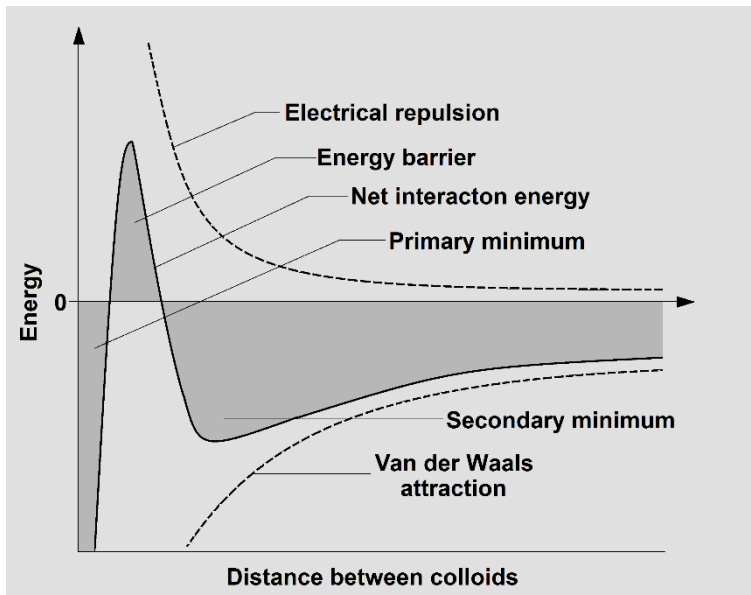
Figure 2.11: The curve illustrates the total energy between to particles when both Van der Waals attractive and double layer repulsive forces are both taken into account.

Figure 2.11 is only a representation of a general case. At very small interparticle distances, the attractive Van der Waals forces dominate, and particles will be tightly bound together. This region is often referred to as the primary minimum or energy trap. As the interparticle distance increases, the net interaction energy may go through a maximum, depending on the system. If this maximum is in the repulsive region, it is referred to as the energy barrier. The height of this barrier represents the stability of the system. For two particles to agglomerate, they must have the required mass and velocity to overcome this barrier. The energy barrier can be manipulated by changing the pH or by adding surfactants. The secondary minimum is a region of net attractive energy. Particles can be trapped in the secondary minimum and form soft agglomerates if they lack sufficient energy to pass the energy barrier. The system does not always have an energy barrier or a secondary minimum. If there is no section of net repulsive energy, the system does not have an energy barrier. Agglomeration is then favored.[21]

2.2.4 Stability factors

Several factors influence the stability of a suspension. The influence of particle size, pH, particle concentration, and complexing agents are discussed in the subsequent sections.

Particle size

Particle size has a large impact on dispersion stability as sedimentation velocity is directly related to particle radius. Larger particles promote faster sedimentation as gravitational forces exceeds the contribution from repulsive forces between particles. Smaller particles give slower sedimentation velocity, but the increase in surface area leads to increased tendency to agglomerate. These soft agglomerates can be broken by mechanical forces, e.g. by ultrasonic treatment.[22] [23] Ultrasonification thus leads to reduced agglomeration and may greatly increase stability of particles dispersed in a medium.

Effect of pH

Attractive Van der Waals forces are the driving force of the formation of agglomerates of particles dispersed in a liquid medium. To stabilize a dispersion, the repulsive forces must be equal to or stronger than the attractive forces, as mentioned in section 2.2.1.

The repulsive forces originate from coulombic repulsion due to electric surface charges on the particles, in this work referred to as the double layer forces. These double layer forces can be manipulated by changing the pH of the suspension. The pH level of pure metallic oxide powder in water is equal to the p.z.c. for the metallic oxide. By adjusting the pH by either basic or acidic additives away from the p.z.c., the double layer forces can be increased to counteract the attractive Van der Waals forces, and stability can be obtained. For TiO_2 the p.z.c. varies slightly with concentration, but is generally close to pH 6.[24]

Another source of repulsion is steric repulsion. Steric repulsion originates from large particles or polymeric chain molecules that adsorbs on the particle. This keeps particles

from getting so close to each other that agglomeration can occur.[25] Higher concentration of particles in a suspension increases the likelihood of particle collision due to Brownian motion. Agglomeration may occur when particles collide. By reducing the amount of particles per volume unit, the amount of particles that collide, and thus the degree of agglomeration, is also reduced.[23] Steric repulsion can be used to counter-act the increased chance of particle collision in suspensions with high concentration of particles.

Complexing agents

Stabilizing a suspension of TiO_2 in a metal nitride solution is more difficult than in water, due to larger amounts of charged ions interacting with dispersion stability. This can be counter-acted by adding complexing agents to neutralize the charged ions. Citric acid, or CA, and EDTA are examples of complexing agents.

CA and EDTA form stable complexes with metal cations. For alkali metals, alkaline earth metals, and aluminum, that have noble gas configurations, the bonding forces between the complexing agents and the cations are purely electrostatic in nature. CA can form both monodentate, bidentate, and tridentate bonds with metal cations, whereas EDTA is a hexadentate complexing agent. This means that both CA and EDTA may form multiple bonds to the cation, which makes for very stable complexes. EDTA is a stronger complexing agent than CA, because EDTA forms multiple types of bonds to metal cations. Both oxygen and nitrogen in EDTA has the ability to form bonds with the cation, while in CA, only bonds between oxygen and the cation may form. Figure 2.12 illustrates how CA and EDTA binds to a cation. in the figure, a bidentate bond between CA and a metal cation is shown. When complexing agents binds to the cations and form chelates, they are partly neutralized. This reduces the overall apparent amount of charged ions in a solution or suspension.[26] [27] [28]
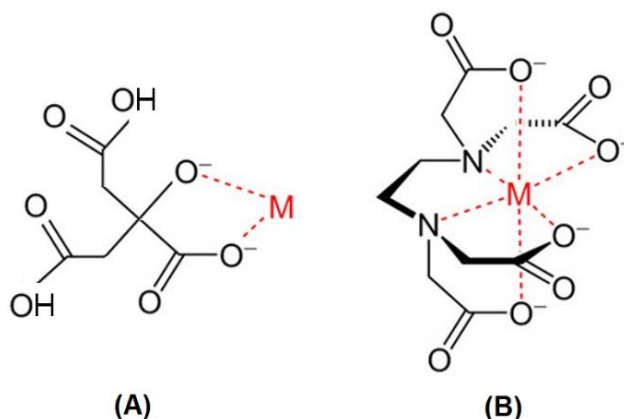

Figure 2.12: Illustration of how CA (A) and EDTA (B) binds to a metal cation.[29]

2.3 Powder synthesis

Several methods can be used to produce ceramic powders. Freeze-drying, Hot Kerosene Drying, Sol-Gel and Spray Pyrolysis are methods that makes it possible to

produce nano-sized particles.[4] All of the mentioned methods start out with either a solution or suspension of precursor metal salts. Depending on the method, different techniques are used to produce the powder. Spray pyrolysis is used to produce the $BaTiO_3$ in this work, through the process described in the following section.

2.3.1 Spray pyrolysis

The term "Spray Pyrolysis" is used in literature for several similar processes, which slightly differ from each other. In this report, the term spray pyrolysis will be used about the process where a true solution, suspension or colloidal dispersion, emulsion or sol is atomized trough a nozzle into a high-temperature heating chamber. The liquid then evaporates and powder is obtained.

M. Ruthner first commercialized spray pyrolysis in the Ruthner process in 1983. It was originally designed for chlorine regeneration in steel production.[30] Since then, the advantages of ceramic powder production through spray pyrolysis has led to the development of several different processes. The key advantages are the versatility in target composition, good stoichiometry control, high purity and narrow particle size distribution of produced powders, with an added benefit of low production cost. The versatility in target composition comes from the large variety of metal salts soluble in either water or organic solvents. Stoichiometry can be controlled by changing the concentration ratio of precursors.

A schematic illustration of the spray pyrolysis equipment used by CerPoTech AS can be seen in Figure 2.13. The precursor solution or suspension is pumped from a container and atomized through a nozzle. The atomized droplets are sprayed into a horizontal furnace with pressurized air flow where the liquid solvent evaporates. The resulting powder is collected in a water-cooled funnel. CerPoTech produces powder using a batch process, but spray pyrolysis can be designed as a continuous process as well.
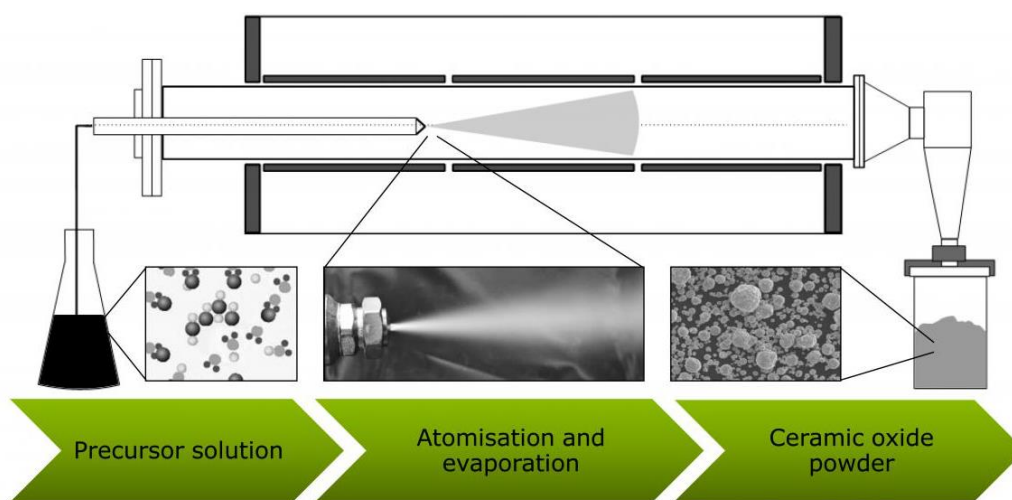

Precursor solution | **Atomisation and evaporation** | **Ceramic oxide powder**

Figure 2.13: Schematic figure of spray pyrolysis equipment used by CerPoTech AS.[31]

Several parameters are important for the resulting purity, particle morphology and particle size. The chemical reactions in the process can be controlled by adjusting atmosphere, temperature, droplet velocity, droplet size, choice of precursors and size of the dispersed particles. The droplet size after atomization is the most influential factor for the particle size of the produced powder. The concept of spray pyrolysis is that one droplet of solute forms one particle when the solvent evaporates. Droplet characteristics depend on the type of nozzle used as well as the solution density, viscosity and surface tension. Atomization occurs when the pressure in the nozzle exceeds the surface tension of the solution. The surface tension is generally less for organic solvents than for water. It is thus easier to obtain smaller droplet sizes for organic solutions than for aqueous solutions.[30] Both organic and aqueous solvents are frequently used, but aqueous solutions are easier to handle, safer, and cheaper than most organic solutions. There is also a wide range of water-soluble metal-salts available. When spraying a suspension, the particle size of the suspended particles will influence the size of the final particles. This is because it is energetically favorable for the solute to precipitate on the surface of the suspended particles than to nucleate and form new particles.

Several different nozzle types exist, giving different droplet sizes and velocities. Higher droplet velocity gives shorter residence time in the furnace. Longer residence time in the furnace leads to a more complete reaction, and thus reduces the need for subsequent heat treatments. The problem with this is that high pressure in the nozzle is often needed to achieve small droplet size. This will in turn increase droplet velocity, and as a consequence reduce residence time. High temperatures and short residence time favors nucleation over particle growth, leading to smaller particles in the end product. The precursors used in the spray pyrolysis process are rarely completely reacted after spraying, due to the relatively short residence times of the particles in the furnace. Subsequent heat treatments (calcination) are often needed to obtain phase-pure powders.

High furnace temperature and short residence time favors the formation of porous particles and hollow shells, due to limited internal diffusion as the solvent evaporates.[30] The hollow shell structures must be ground during a subsequent milling step.[31]

2.4 Particle size calculations

There are several different methods to calculate average particle size of powders. One method is to calculate the crystallite size from the peak broadening in an x-ray diffractogram. P. Scherrer demonstrated in 1918 that when a randomly oriented mass of crystals is exposed to monochromatic radiation, the diffracted beam is broadening with decreasing crystallite size.[32] This is the basic principle behind the Scherrer formula that can be written as:

$$B(2\theta) = \frac{K\lambda}{L \cdot \cos(\theta)}$$

Where B is the peak width, K is the Scherrer constant, λ is the wavelength of the radiation, L is the crystallite size, and θ is the Bragg angle. The constant K has been evaluated extensively[32] [33], and common values for K can be seen in Table 2.1. The full width at half maximum, or FWHM-method uses the peak width at the half maximum intensity of the peak for the value of B. This is the method used in the calculations of the Scherrer particle size in section 4.4.

Table 2.1: Common values for K for given methods of defining B.[34]

Method for B	Values of K
FWHM of spherical crystals with cubic symmetry	0.94
Integral breadth of spherical crystals with cubic symmetry	0.89

Another method of finding average particle size is by BET (Brunauer-Emmet-Teller) analysis. In BET analysis, specific surface area of powder is measured by a gas adsorption method. Nitrogen gas is adsorbed on the particle surfaces of the powder. The amount of adsorbed gas is measured, and the particle size can then be calculated. Particle size can also be determined from SEM imaging. Using this method, grain size in pressed and sintered pellets is also obtainable.

2.5 Pressing of pellets

To characterize piezoelectric properties, it is necessary to press pellets of the powders. There are several methods to produce pellets. In this work, a hydraulic press is used. The powder is placed in a die as shown in Figure 2.14. Density will increase with increasing pressure until a certain point. Any excess pressure leads to deformation in the pellet. Deformation in the green body might lead to cracking during sintering, and too little pressure gives poor density of the final samples. To achieve maximum green body density, multiple pellets can be pressed and the green body density measured as a function of pressure. The resulting pressure-density curve can then be used to decide the optimal pressure. The optimal pressure for pressing is dependent on particle size and size distribution, as well as of course particle chemistry. Small particle size leads to closer packing and as such higher green body density, while narrow particle size distribution might reduce green body density as there are no smaller particles to fill the gaps between larger particles.[4]

Die fill stage

Compaction

Upper
punch

Powder

Die

Lower
punch

"Green"
compact

Part ejection
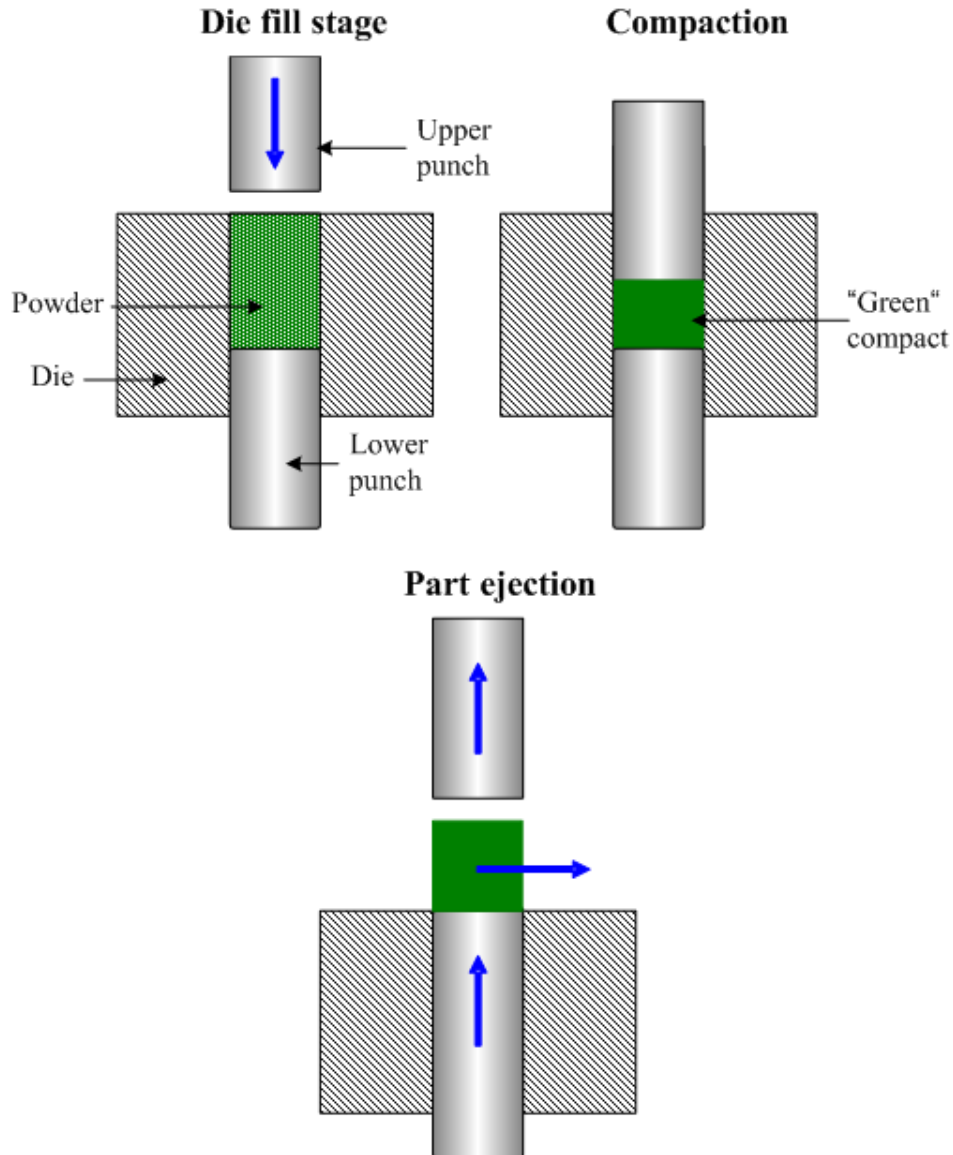
Figure 2.14: Illustration of how ceramic powders can be pressed into green body pellets using a hydraulic pressing tool. Powder is put in the die, and pressure is applied. The pressed pellet is then ejected from the die.[35]

2.6 Sintering behavior

There are several techniques to achieve densification of a ceramic green body, including conventional sintering and hot pressing. In this work, conventional sintering has been used. For sintering to occur, a material transport mechanism, and a source of energy to activate and sustain this material transport, must be present. Several mechanisms for material transport exist, but the most important ones are diffusion and viscous flow. Material transport during sintering can occur in vapor, liquid or solid-state. Solid state sintering is the most important mechanism in this work. In solid-state sintering, material

transport occurs by volume diffusion along grain boundaries, or diffusion along material surfaces. Diffusion along grain-boundaries leads to volume shrinkage. The driving force for this kind of diffusion is the chemical potential difference between free surfaces and points of contact between grains or particles.

The physical changes that occur in a material during sintering is often divided into three stages. In the first stage, the particles in the material rearranges and neck formation occurs as shown in Figure 2.15 (A).
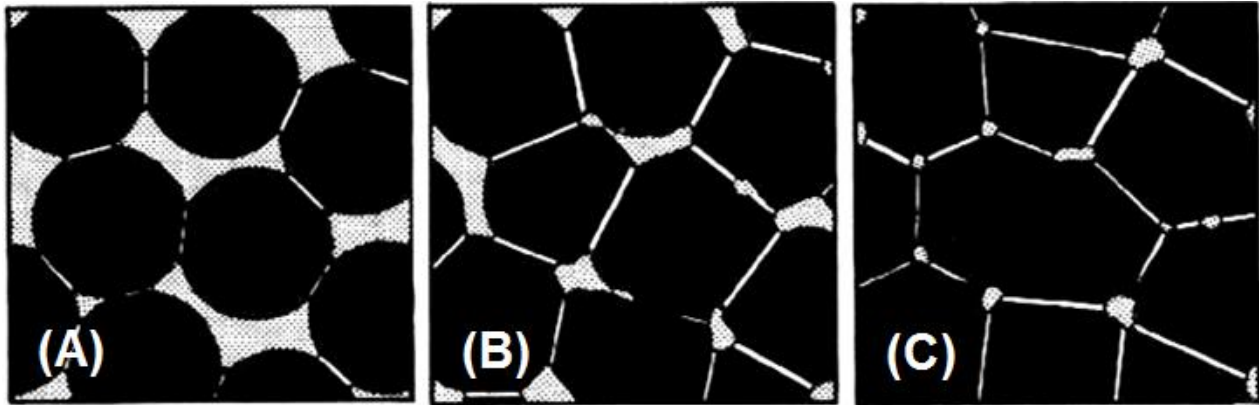

Figure 2.15: Illustration of neck formation, grain growth, and pore elimination during the first (A), second (B), and third (C) stages of sintering.[36]

The rearrangement consists of particle movement or rotation to increase the amount of contact points between particles. Bonding occurs at these contact points, and allows for material transport which leads to necking. Porosity is still present at this stage.

The second stage consists of neck growth, grain boundary lengthening, porosity reduction and volume shrinkage. This is illustrated in Figure 2.15 (B). As the grains move closer together, they are more firmly bonded because grain boundaries lengthen, volume shrinkage occurs and porosity is reduced. Some grain growth also occurs.

In the final stage, grain growth dominates. As the grains grow, porosity is reduced and ultimately eliminated, as shown in Figure 2.15 (C). This happens as grain boundaries lengthen, reducing the size of the pores and ultimately eliminating them completely.

Knowledge of the material to be sintered is important in order to choose a suitable sintering program. This is to avoid secondary phase formations, melting and loss of stoichiometry during sintering. When densification and pore elimination is the main goal, the maximum sintering temperature must be chosen to be high enough for densification to occur without formation of secondary phases. The time at maximum temperature and heating rate also influence the resulting density, phase purity, and grain size. Crucible material is another factor that needs to be considered. Al_2O_3 is a common crucible material, but may react with the material to be sintered. This can be avoided by using e.g. platinum crucibles.[4]

2.7 Existing methods for BaTiO$_3$ synthesis

Several synthesis methods for BaTiO$_3$ has been reported in literature. The common precursors for production of BaTiO$_3$ by spray pyrolysis is titanium isopropoxide and barium nitrate. In this case, titanium isopropoxide is in aqueous solution with barium nitrate. The resulting solution is very acidic, due to the large amount of citric acid required to dissolve titanium isopropoxide.

Solid-state synthesis of BaTiO$_3$ from BaCO$_3$ and rutile TiO$_2$ have been reported. Buscaglia et. Al.[37] reported synthesis of BaTiO$_3$ with an average particle size of 100 nm and size distribution d(50)= 270 nm in 2005. The precursor rutile TiO$_2$ (70 nm) and BaCO$_3$ (50 nm) was calcined at 800 °C for 8 hours to obtain these results. Zhao et Al.[38] also reported synthesizing BaTiO$_3$ by solid-state synthesis in 2015. However, the reported particle size was much larger, averaging at 400 nm.

Synthesis of BaTiO$_3$ through a wet chemical synthesis was reported by Roh et. Al.[39] in 2015. The powder was synthesized using a liquid precursor method, impregnating titanium-lactate complexes into starch and then drying before firing at temperatures ranging from 600-1000 °C. The resulting average particle size varied from 25 nm to 50 nm depending on which concentrations and molar ratios were used.

There is no mention of synthesis of BaTiO$_3$ from spray pyrolysis using dispersed anatase TiO$_2$ as the source of titanium. This works aims to investigate the possibility for this as a new synthesis route for BaTiO$_3$-nanoparticles.

3 Experimental

The chemicals and abbreviations used in this work are listed in Table 3.1.

Table 3.1: The chemicals and abbreviations used in this work.

Chemical	Details	Abbreviation
Barium nitrate	Alfa Aesar, 99 %[40]	$Ba(NO_3)_2$
Titanium dioxide	Sigma-Aldrich, < 25 nm, 99.5 %[41]	TiO_2
EDTA	VWR Chemicals, 98 %	EDTA
Citric acid	Ensign, 99.5 %	CA
Ammonium solution	Merck, 65 %	NH_4OH
Nitric acid	Merck, 25 %	HNO_3
Darvan C-N	Vanderbilt minerals	Darvan C-N
Dolapix A 88	Zschimmer & Schwarz	Dolapix A 88

During this work, three synthesis routes were used to produce the $BaTiO_3$ powder. The abbreviations BTO-a, BTO-c, and BTO-n has been used to describe them. These abbreviations refer to $BaTiO_3$-alkoxide, $BaTiO_3$-complexed, and $BaTiO_3$-non-complexed respectively. The compositions of each synthesis route is explained in Table 3.2.

Table 3.2: Overview of the three synthesis routes and what precursors and complexing agents were used in which route.

Chemical	BTO-a	BTO-n	BTO-c
$Ba(NO_3)_2$	Yes	Yes	Yes
TiO_2	No	Yes	Yes
Titanium isopropoxide	Yes	No	No
EDTA	Yes	No	Yes
CA	Yes	No	Yes

3.1 Precursor suspensions

Preliminary experiments were done to find suitable pH-levels for a stable TiO_2-dispersion in water. Based on the results from these tests, the optimal pH-level of the suspensions was decided to be around 8.

To prepare TiO_2-suspensions, NH_4OH-solution was added to distilled water (1.0 L) to adjust the pH to 8, and TiO_2 (34.25 g) was added. The suspension was stirred for 30 minutes and then put in an ultrasonic bath for 30 minutes. This method of producing the precursor TiO_2 suspension was used in both the BTO-c and the BTO-n synthesis routes explained in Table 3.2. Figure 3.1 shows the flow chart for the production process of the BTO-c and BTO-n suspensions.

3.1.1 BTO-a precursor solution

BTO-a is a reference solution prepared by CerPoTech AS using their conventional synthesis route for $BaTiO_3$. It was prepared by dissolving titanium isopropoxide in water by adding CA to obtain acidic conditions, then adding a barium nitrate solution complexed with EDTA and CA.

3.1.2 BTO-n precursor solution

In the BTO-n suspension, $Ba(NO_3)_2$ (112.08 g) was dissolved in distilled water (3.5 L). The pH was then adjusted to 8 by adding NH_4OH. The TiO_2-suspension made earlier, see section 3.1, was then added to the barium solution while keeping careful control of the pH, and adjusting with NH_4OH to keep the pH at 8, see Figure 3.1. The final volume of the suspension was 5.0 L with a total theoretical weight of 100 g $BaTiO_3$.

3.1.3 BTO-c precursor solution

The process and ratio of complexing agents to cations used when making the BTO-c solution in this experiment is the same process used by M. Sletnes in her Ph.D.-thesis[42] for complexing barium with the use of CA and EDTA. The molar ratio $Ba(NO_3)_2$:EDTA:CA used is 1:1:2. This method is described in Figure 3.1 and in the following section.

In the BTO-c suspension, EDTA (125.32 g) was dissolved in distilled water (3.5 L) by adding small amounts of NH_4OH. $Ba(NO_3)_2$ (112.06 g) was then added and the solution was stirred until all $Ba(NO_3)_2$ was dissolved. CA (164.76 g) was added, stirred until dissolved and the pH was adjusted to 8 by adding NH_4OH. The TiO_2-dispersion made earlier, see section 3.1, was then added to the barium solution while keeping careful control of the pH, and adjusting with NH_4OH when needed. The final volume of the suspension was 5.5 L with a total theoretical weight of 100 g $BaTiO_3$.
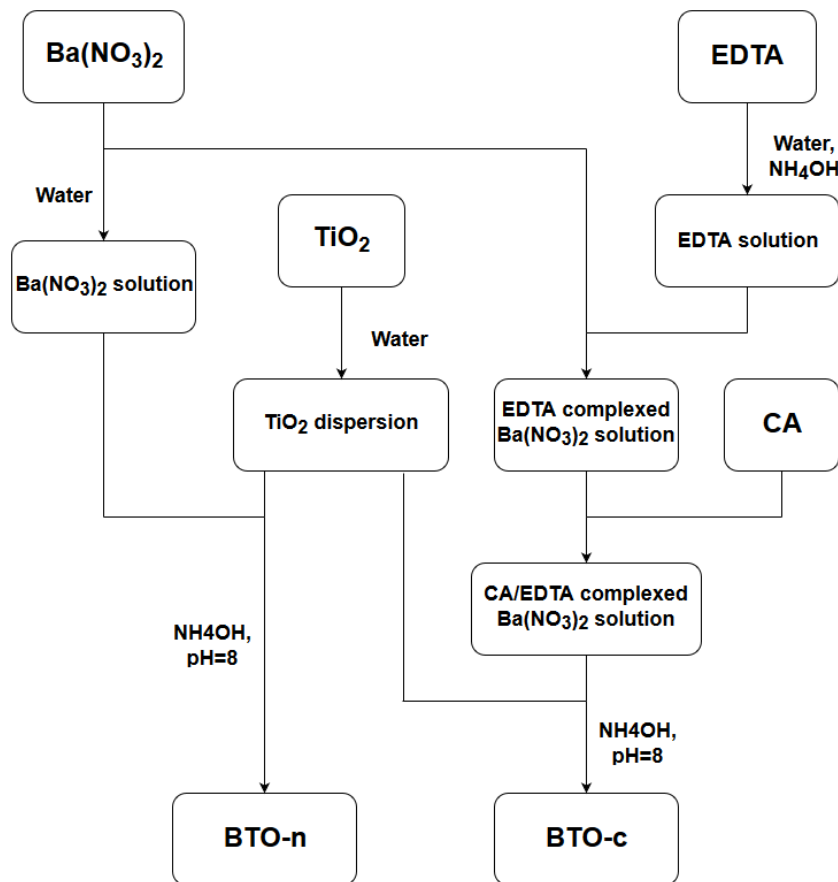
Figure 3.1: Flowchart illustrating the two synthesis routes BTO-n and BTO-c.

3.2 Spray pyrolysis of suspensions

The spray pyrolysis was done at CerPoTech AS in Trondheim, using pilot-scale spray pyrolysis equipment. The suspensions were stirred continuously while being pumped into the spray-pyrolysis furnace, in an attempt to counter sedimentation due to the poor stability of the suspensions. The furnace temperature was set to 1000 °C.

3.3 Calcination

Different calcination programs were investigated, but all powders used for subsequent analysis was calcined at 800 °C for 14 hours with a heating rate of 200 °C/hour, as this was found to give the best result. An overview of all the different calcination programs investigated is given in Appendix A.

3.4 Characterization of powders

The as synthesized and calcined powders where characterized by XRD (X-ray Diffraction) (D8 Advance Da Vinci 1, Bruker, Germany). The instrument used Cu-Kα (wavelength λ = 1,5418 Å) radiation and LynxEyeTM SuperSpeed detectors.

The powders were also characterized by SEM (Scanning Electron Microscope) imaging (Zeiss Ultra 55, Zeiss, Germany) using a secondary electron detector, with 5 mm working distance and an accelerating voltage of 5 kV.

The powders were wet milled in ethanol on a ball mill for 48 hours using YSZ (yttria stabilized zirconia) milling balls. The milled powders were characterized by SEM-imaging and the specific surface area was measured by BET analysis (TriStar 3000, Micrometrics, U.S.), using nitrogen as the adsorption gas.

The BTO-c powder was characterized by TGA (Thermogravimetric analysis) (STA449 jupiter, NETZSCH, Germany). Details about the program that was used and results of the TGA can be seen in Appendix C.

3.5 Suspension stabilization

Poor stability of the suspensions was one of the problems encountered during the spray pyrolysis of the suspensions in section 3.1. To address this issue, tests were carried out to improve the stability. Testing on both TiO_2 dispersed in water and complete system tests with BTO-c and BTO-n solutions were conducted. Different dispersants and varying concentrations of powder and dispersant were tested. The pH levels were chosen based on the results from the dispersion tests done by the author in 2015.[1]

3.5.1 TiO$_2$ dispersions

Dispersions of anatase TiO_2 powder were prepared in two steps. First, specific amounts of dispersant (see Table 3.3) was added to water (100 ml) while stirring the solution continuously. Then, specific amounts of TiO_2 powder were added to the dispersant solution while stirring. The pH was then adjusted to the appropriate level by adding NH_4OH and HNO_3. Each sample was then given ultrasonic treatment using an ultrasonic bath for 30 minutes. 10 ml of each finished sample was transferred to a measuring cylinder. A photo was taken every 20 minutes for the first hour, and then after 24 hours. This data was used to decide the height of the sedimentation layer at a given time for the different samples. Figure 3.2 illustrates the experimental setup of the measuring cylinders with dispersion.

Table 3.3: Table of the different pH values, amounts of TiO2, and types of dispersant used in the dispersion stability tests of TiO2 in water.

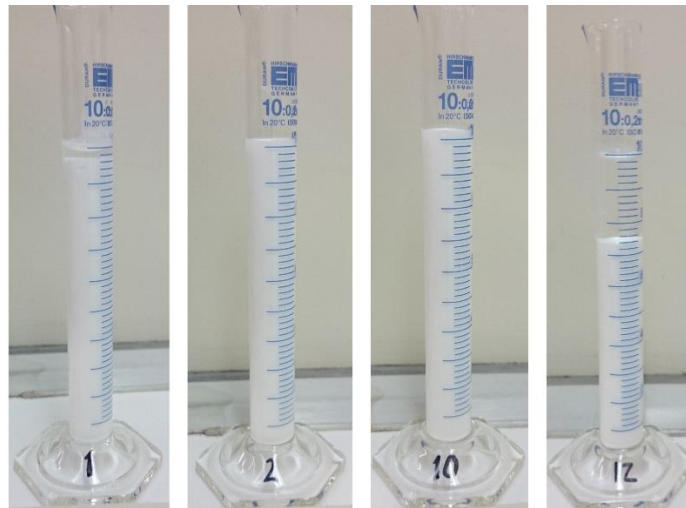| pH	Sample number	Concentration [g/100 ml water]		
		TiO_2	Darvan C-N	Dolapix A 88
	1	2.75		
	2	2.75	1.00	
	3	2.75		1.00
	4	2.00		
7	5	2.00	1.00	
	6	2.00		1.00
	7	1.00		
	8	1.00	1.00	
	9	1.00		1.00
	10	2.75		
	11	2.75	1.00	
	12	2.75		1.00
	13	2.00		
8	14	2.00	1.00	
	15	2.00		1.00
	16	1.00		
	17	1.00	1.00	
	18	1.00		1.00

Figure 3.2: Examples of the experimental setup of measuring cylinders with dispersion

3.5.2 Complete system testing

To test the stability of the complete systems, TiO_2 powder was dispersed in both simple $Ba(NO_3)_2$-solutions (BTO-n) and in complexed $Ba(NO_3)_2$-solutions (BTO-c) where the barium ions were complexed with EDTA and citric acid (CA), as in section 3.1.

For BTO-n, this was done by dissolving $Ba(NO_3)_2$ (9.00 g) in water (150 ml). Then the pH was adjusted by addition of NH_4OH and HNO_3. TiO_2-dispersions were prepared as in the previous section by adding Darvan C-N (1.00 g) to water (100 ml) and stirring for 5 minutes. Then, TiO_2 (2.75 g) was added to the solution. The pH was then adjusted to 8 by addition of NH_4OH and HNO_3. The TiO_2 dispersions were then given an ultrasonic treatment for 30 minutes, before being added to the Ba-solutions. Finally, the complete suspensions were stirred for 5 minutes. 10 ml of each suspension was transferred to a measuring cylinder. A photo was taken after 60 minutes and after 24 hours. This data was used to determine the relative stability of the systems.

For the BTO-c solutions, EDTA (10.07 g) was dissolved in 200 ml of water by adjusting the pH to 8 with the addition of NH_4OH-solution. $Ba(NO_3)_2$ (9.00 g) was then added and the solution was stirred until all was dissolved. CA (13.23 g) was then added and the pH adjusted with NH_4OH and HNO_3. TiO_2-dispersions was prepared as in the previous section. The pH was again adjusted to 8 by adding NH_4OH and HNO_3. The TiO_2 dispersions were given an ultrasonic treatment for 30 minutes, before being added to the Ba-solutions. Finally, the complete suspensions were stirred for 5 minutes. 10 ml of each suspension was transferred to a measuring cylinder. A photo was taken after 60 minutes and after 24 hours.

3.5.3 Varying the dispersant amount

Complete system tests of the BTO-c synthesis route with varying amounts of dispersant were carried out. The amounts of $Ba(NO_3)_2$, TiO_2, EDTA and CA are the same as for the previous complete systems tests, and are listed in Table 3.4 along with the amount of dispersant added. The pH of the suspensions was adjusted to 8 as for the previous tests. The samples were made as in the previous section, the only change being the concentration of dispersant added.

Table 3.4: Table of the different amounts of Ba(NO3)2, TiO2, EDTA, CA, and Darvan C-N used in the suspensions.

Sample number	Ba(NO3)2 [g/200 ml water]	EDTA [g/200 ml water]	CA [g/200 ml water]	TiO_2 [g/100 ml water in TiO_2 dispersion]	Concentration of Darvan C-N [g/100 ml water in TiO_2 dispersion]
1	9.00	10.07	13.23	2.75	1.00
2	9.00	10.07	13.23	2.75	2.00
3	9.00	10.07	13.23	2.75	3.00
4	9.00	10.07	13.23	2.75	3.00
5	9.00	10.07	13.23	2.75	5.00
6	9.00	10.07	13.23	2.75	5.00

It is important to note that the dispersant is added to the TiO_2-dispersion before it is mixed with the barium solution. Sample 4 and 6 were given an additional ultrasonic treatment for 20 minutes after mixing the complexed barium solutions and the TiO_2-

dispersions, in order to investigate the effect of additional ultrasonic treatments on suspension stability.

3.6 Pressing and sintering

The calcined and milled powders from all three synthesis routes were pressed to pellets using a hydraulic c-press and a 10 mm die. Stearic acid was used as a lubricant. Table 3.5 lists the pressing conditions. The pressed pellets were then sintered at different conditions as indicated in Table 3.6.

The densities of the sintered samples were measured using the Archimedes' method with isopropanol as the immersion liquid, according to the international standard ISO 5017.

Table 3.5: List of the different loads used during pressing in tons and in MPa. The die used had an inner diameter of 10 mm.

Pressure [Tons]	Pressure [MPa]
0.8	100
0.9	112
1.2	150
1.4	175
2.4	300
3.4	425

Table 3.6: Table showing the different sintering programs used for the different powders, and also what type of crucible was used.

Powder type	Max. sintering temperature [°C]	Heating rate [°C/hour]	Time at max. temperature [hours]	Crucible material
	1200	200	2	Alumina
BTO-a	1200	200	4	Platinum
	1300	200	2	Platinum
	1350	200	2	Platinum
	1200	200	4	Alumina
BTO-c	1200	600	4	Alumina
	1300	600	2	Platinum
	1300	600	4	Platinum
	1300	600	1	Alumina
BTO-n	1300	600	1	Platinum
	1300	600	2	Alumina
	1300	600	4	Platinum

3.7 Piezoelectric properties

Only samples sintered at 1300 °C for 4 hours in platinum crucibles were prepared for piezoelectric testing due to low density for other sintering programs.

To prepare samples for piezoelectric testing, the surfaces were polished with SiC paper on both sides until reflective, with final grain size of 5 μm. Both sides of the samples where then coated with gold using a sputter coater (s150B, Edwards, United Kingdom). The samples were coated using a voltage of 20 kV for 4 minutes. The edges of the samples were then polished to remove the contact between the top and bottom sides. The gold serves as electrodes on either side of the samples during testing. The piezoelectric properties of the prepared samples were then tested using a commercial TF2000 system (AixACCT, Aachen, Germany), with a high voltage amplifier (TREK 610e, TREK Inc., United states). The measurements were performed at 1 Hz with no pre-polarization pulse. This setup utilizes the converse piezoelectric effect, applying an electric potential and measuring the resulting mechanical displacement.

3.8 SEM and EDS of sintered samples

Only samples sintered at 1300 °C for 4 hours in platinum crucibles were prepared for SEM and EDS due to low density for other sintering programs.

To prepare samples for SEM (Scanning Electron Microscope) and EDS (Energy-Dispersive Spectroscopy), the surfaces were polished with SiC paper on one side until reflective, with final grain size of 5 μm, and then thermally etched in a furnace at 1250 °C for 5 minutes using a heating- and cooling rate of 600 °C/hour. The samples were then coated with gold as in section 3.7, but with a voltage of 15 kV for 30 seconds. SEM imaging (Zeiss Ultra 55, Zeiss, Germany) was performed using secondary electron and in-lens detectors, with 3-5 mm working distance and an accelerating voltage of 5 kV. EDS was performed using a SEM (S-3400N, Hitachi, Japan) using secondary electron, backscatter electron, and x-ray detectors, with 10 mm working distance and 60 kV accelerating voltage.

3.9 Viscosimetry

The viscosity of one of the BTO-c suspension samples was measured using a rheometer (HAAKE MARS, Thermo Fisher Scientific, United states). The viscosity was compared to the viscosity of a commercial TiO_2-dispersion (Aerodisp w 740x, Evonik Industries, Germany).

4 Results

4.1 Yield of spray pyrolysis

The resulting weight of the as synthesized powders from the BTO-n and BTO-c synthesis routes after the spray pyrolysis can be seen in Table 4.1. Both synthesis routes had a theoretical yield of 100 g $BaTiO_3$.

Table 4.1: Total weight of powders obtained from the spray pyrolysis. Both synthesis routes had a theoretical weight of 100 g product $BaTiO_3$.

Synthesis route	Weight of powder [g]
BTO-n	75
BTO-c	195

It should be noted that white powder was noticed in the container with the initial suspensions after spraying, indicating sedimentation of TiO_2-powder due to the instability of the suspensions. This could explain the weight loss of the BTO-n powder. The weight of the BTO-c powder can to some degree be explained by the fact that the barium nitrate reacted to barium carbonate during spraying. This can be seen from the XRD diagrams of the BTO-c powder in Appendix A. However, since the BTO-c powder only lost 15.3 % of its weight during calcination (see Table A.1), it is probable that a lot of the weight in the BTO-c powder after spraying comes from moisture present after production. This water must then have evaporated during storage, before calcination.

4.2 Phase purity of powders

XRD was used to identify the phases present in the as synthesized and calcined powders of all synthesis routes. The XRD-diagrams of the powders obtained from the three synthesis routes calcined at 800 °C are compared in Figure 4.1. These were the most phase-pure. However, small amounts of a secondary phase, believed to be

29

Ba_2TiO_4, was present in the BTO-n powder. The XRD diagrams of the as synthesized powders and powders calcined at 600 °C and 700 °C can be found in Table A.1.
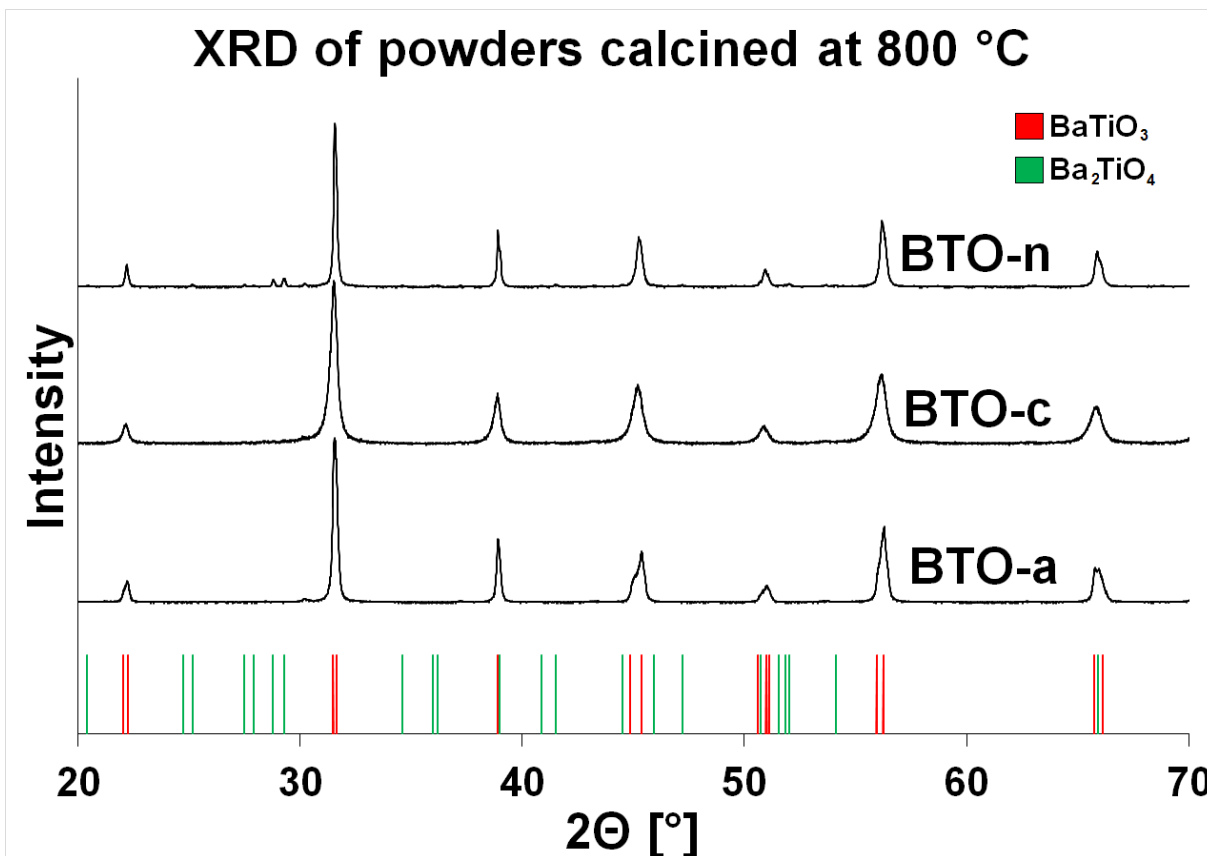

Figure 4.1: Powders calcined at 800 °C for 6 hours. The BTO-n powders showed small peaks at around 28°, matching the peaks of the secondary phase Ba_2TiO_4.[1]

4.3 Morphology

The morphology of the particles of the as synthesized powders as well as the particles of the powders calcined at 800 °C before and after milling were characterized by SEM. The as synthesized powder is discussed in Appendix B.

Images of calcined powders from all synthesis routes before and after milling are shown in Figure 4.2. The soft agglomerates and porous particles in the calcined powders, seen in Figure 4.2 (A-C), had been crushed in the milling process. The resulting powder consisted of small, approximately spherical particles, with the exception of the BTO-n powder. For the BTO-n powder, it was clear that some larger, non-spherical particles were still present after the milling procedure, see Figure 4.2 (E).
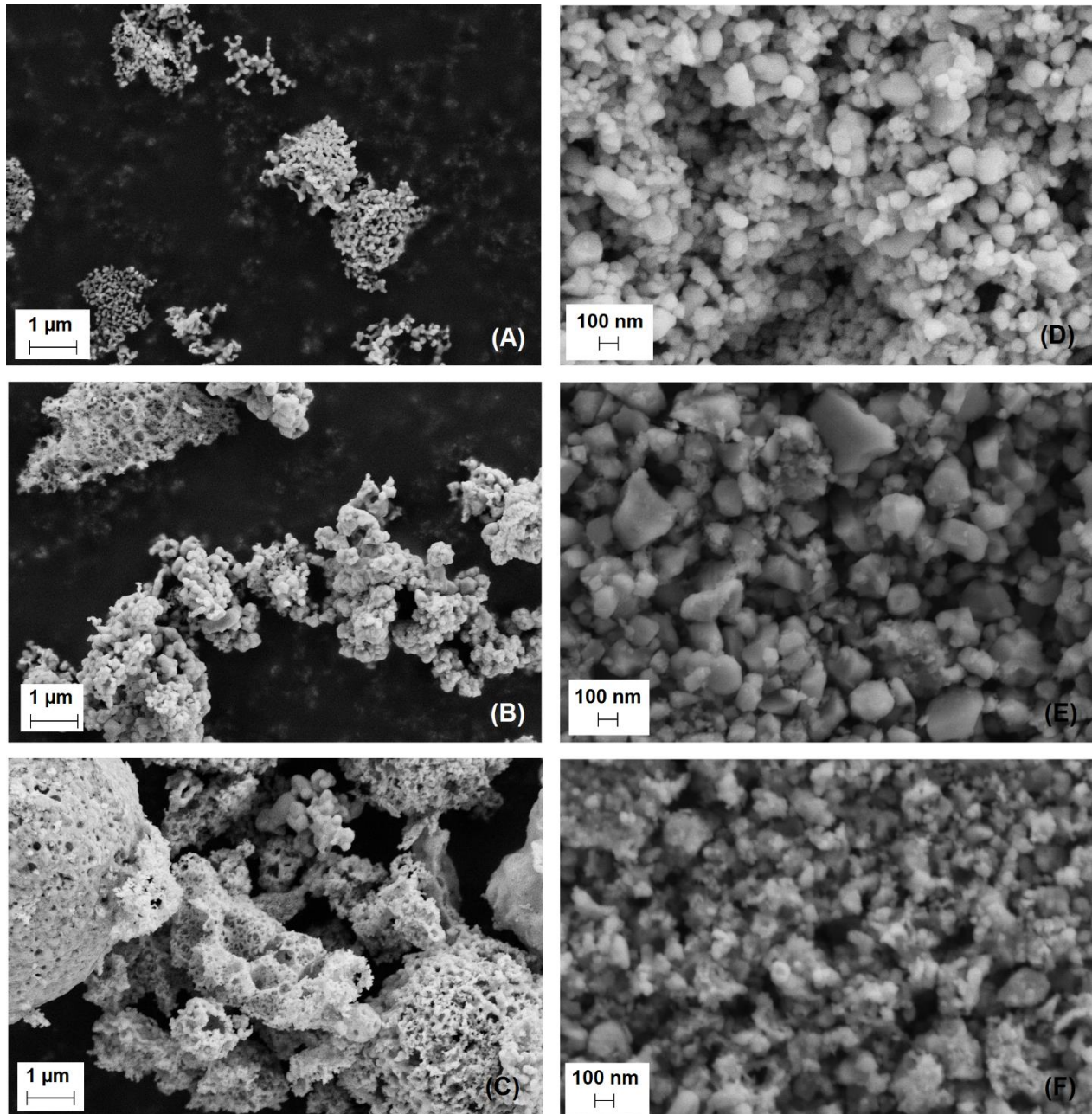
Figure 4.2: Powders from all synthesis routes calcined at 800 °C for 6 hours, before and after milling for 48 hours. BTO-a after calcining (A) and after milling (D). BTO-n after calcining (B) and after milling (E). BTO-c after calcining (C) and after milling (F). It is important to notice the different scale bars in samples before and after milling.[1]

4.4 Particle size

The specific surface area of the powders from all synthesis routes were calculated from the results of the XRD using the Scherrer equation and the FWHM-method. The crystallite size was calculated from the width of the peak with the highest intensity, as seen in Figure 4.1. It is clear that the width of peak in the BTO-c XRD-pattern is the

broadest, thus it is as expected that the BTO-c synthesis route yielded the smallest crystallite size.

The specific surface area was also measured by BET-analysis. The average particle size of each synthesis route was calculated for both methods assuming spherical particles if even distribution. The results of both calculations can be seen in Figure 4.3. It should be noted that the BET particle size of the BTO-n powder was measured to be smaller than the calculated Scherrer particle size. This is an unusual result, but could be due to the secondary phase formation of Ba_2TiO_4 in the BTO-n powder. Another explanation is that the assumption of spherical particles in the milled BTO-n powder is wrong, as seen in Figure 4.2 (E). There is also a substantial margin of error in the Scherrer results. The results indicate that the particles are monocrystalline, due to the similarity of the particle diameter from BET and XRD. The average particle sizes are in the range of 50-100 nm.
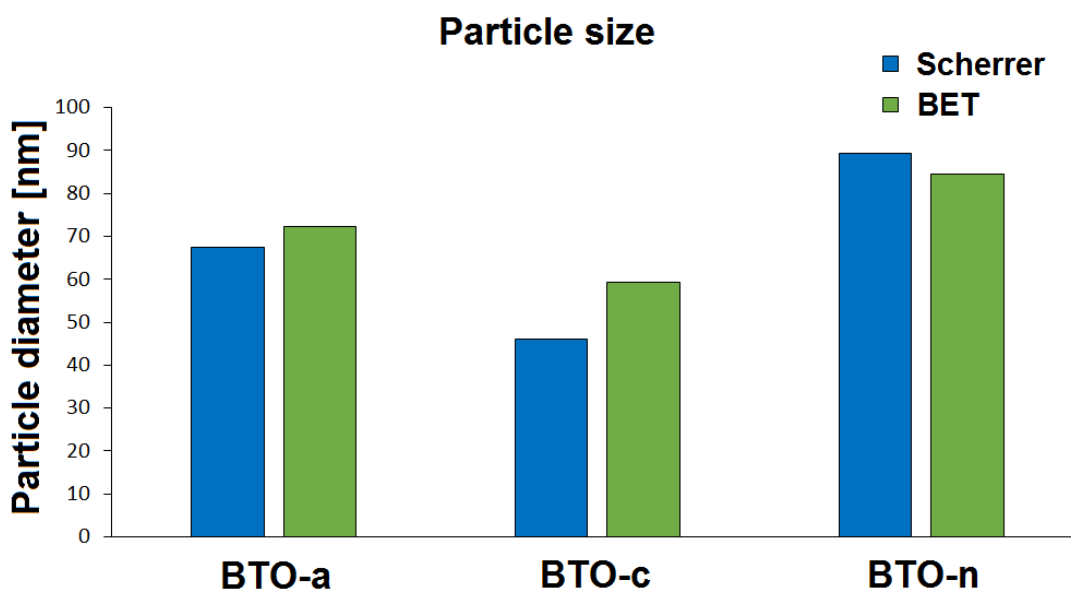

Figure 4.3: Average particle size of the produced powders calculated from XRD-results using the Scherrer method, and from the specific surface area measured by BET-analysis.

4.5 Suspension stabilization

4.5.1 TiO$_2$ dispersions

The results of the stabilization testing of anatase TiO$_2$- powder in water in pH 7 and 8 is given in Figure 4.4. The figure shows the height of the border between the cloudy region with dispersed particles and the clear water, as can be seen in Figure 3.2. This height is given after 24 hours. The sample compositions can be seen in Table 4.2. Samples 2, 5, 8, 11, 14, and 17 were fully dispersed for both pH values, meaning that the dispersions were stable even after 24 hours. In fact, they were stable for several weeks. The stable samples all contain the Darvan C-N dispersant. Further testing of suspension stability was conducted using only the Darvan C-N dispersant.
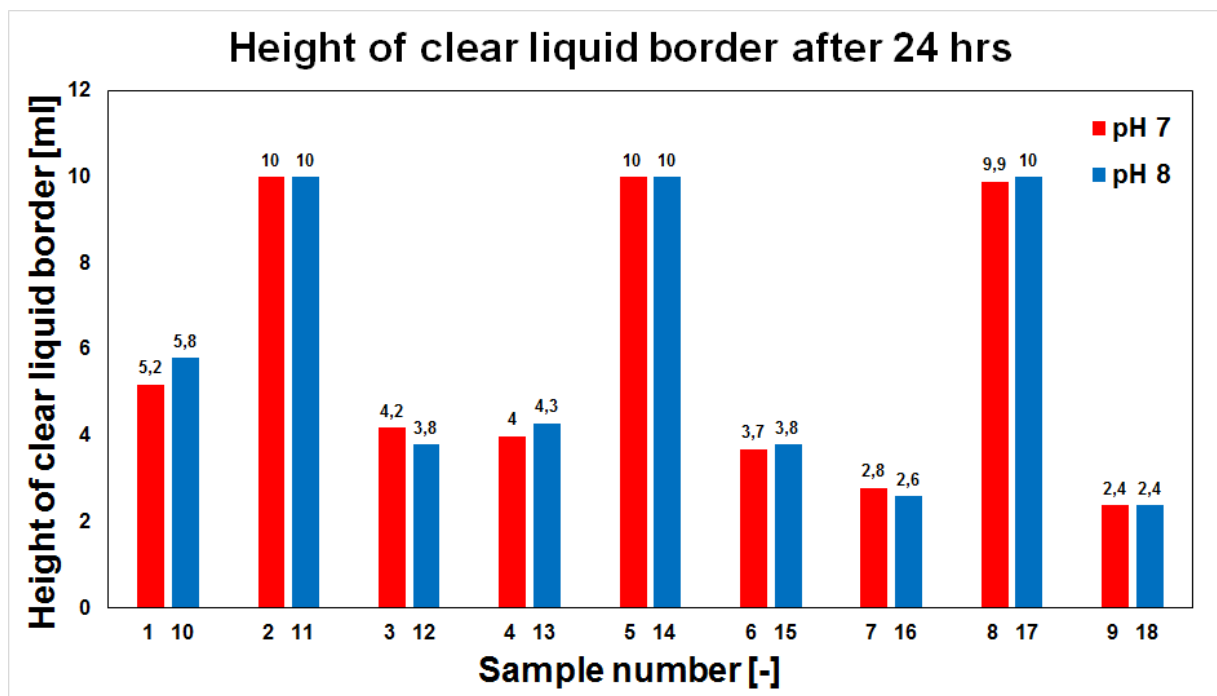

Figure 4.4: Height of clear liquid border indicates the height of the border between the clear water and the cloudy area of dispersed particles in the measuring cylinder. Samples 2, 5, 8, 11, 14, and 17 had no such border, meaning that particles were dispersed in the entire liquid solvent, and the dispersions were stable.

The natural pH of the BTO-c suspensions was closer to 8 than 7, and since there was no clear distinction in stability between samples at pH 7 and 8, pH 8 was chosen for further testing due to convenience.

Table 4.2: Table of the different pH values, amounts of TiO_2, and types of dispersant used in the dispersion stability tests of TiO_2 in water.

pH	Sample number	Concentration [g/100 ml water]		
		TiO₂	Darvan C-N	Dolapix A 88
	1	2.75		
	2	2.75	1.00	
	3	2.75		1.00
	4	2.00		
7	5	2.00	1.00	
	6	2.00		1.00
	7	1.00		
	8	1.00	1.00	
	9	1.00		1.00
	10	2.75		
	11	2.75	1.00	
	12	2.75		1.00
	13	2.00		
8	14	2.00	1.00	
	15	2.00		1.00
	16	1.00		
	17	1.00	1.00	
	18	1.00		1.00

4.5.2 Complete system testing

The complete system testing was done in two stages. In the first stage, the two synthesis routes BTO-c and BTO-n were compared. Figure 4.5 shows the results from the testing after 24 hours. After 24 hours, both suspensions were fully sedimentated, indicating poor suspension stability. The sedimentation layer in the BTO-c suspension was about half the height of the sedimentation layer in the BTO-n suspension. This indicates that the particles in the BTO-c suspension are closer packed, and thus less agglomerated. Based on these results, further testing of the suspension stability was focused on the BTO-c route.
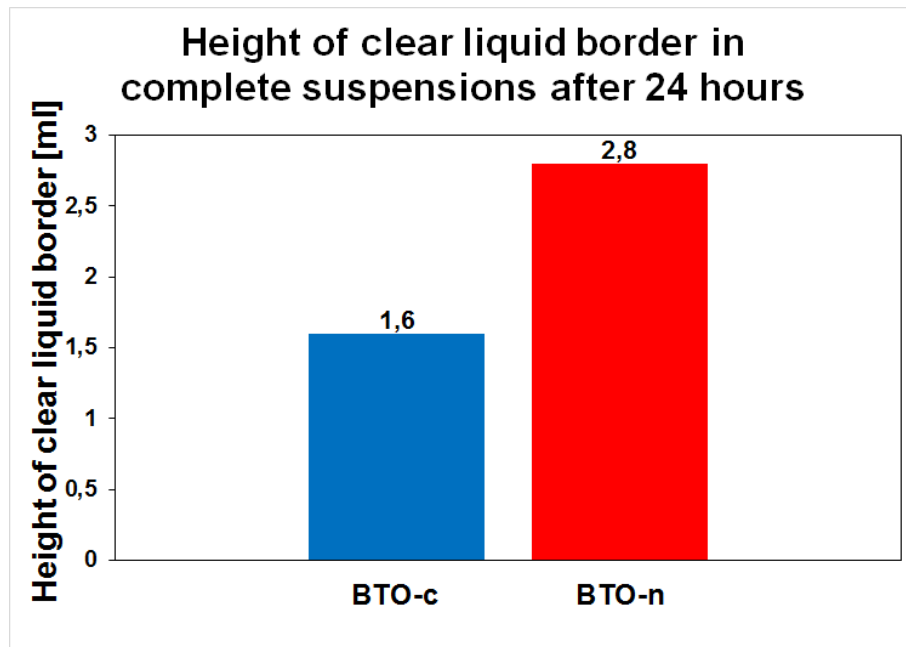
Figure 4.5: Height of clear liquid border after 24 hours for BTO-c and BTO-n suspensions.

4.5.3 Varying the dispersant amount

The testing of the BTO-c proceeded, and varying compositions with regards to amount of dispersant were tested. The results from this testing can be seen in Figure 4.6. The sample compositions are listed in Table 4.3.
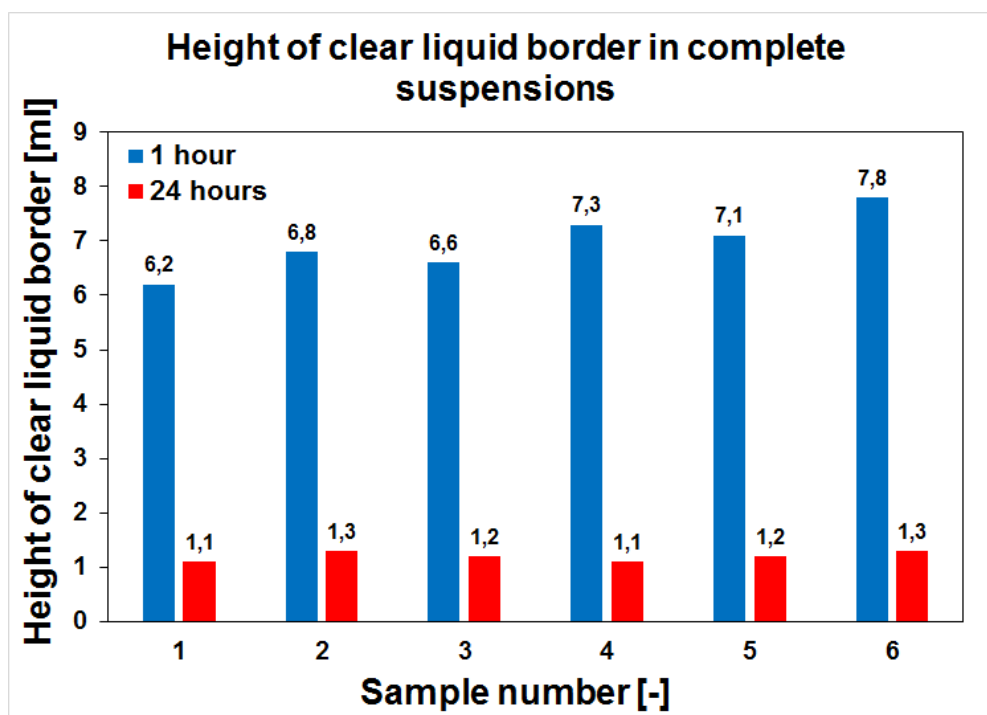

Figure 4.6: Suspension stability of BTO-c suspensions with pH 8 with different amounts of dispersant.

Table 4.3: Table of the different amounts of Ba(NO$_3$)$_2$, TiO$_2$, EDTA, CA, and Darvan C-N used in the suspensions.

Sample number	Ba(NO3)2 [g/200 ml water]	EDTA [g/200 ml water]	CA [g/200 ml water]	TiO$_2$ [g/100 ml water in TiO$_2$ dispersion]	Concentration of Darvan C-N [g/100 ml water in TiO$_2$ dispersion]
1	9.00	10.07	13.23	2.75	1.00
2	9.00	10.07	13.23	2.75	2.00
3	9.00	10.07	13.23	2.75	3.00
4	9.00	10.07	13.23	2.75	3.00
5	9.00	10.07	13.23	2.75	5.00
6	9.00	10.07	13.23	2.75	5.00

4.6 Green body densities of pressed pellets

The resulting green body densities for the BTO-c powder at different pressing conditions are listed in Table 4.4. The densities are given as percentage of theoretical density for BaTiO$_3$, which is 6.02 g cm^{-3}. The sample pressed at 425 MPa was destroyed due to too high pressure leading to deformation. Maximum load before deformation occurred was determined to be around 150 MPa. This load was then used for all samples that were sintered and analyzed.

Table 4.4: List of green body densities for BTO-c samples pressed at the given loads. The sample pressed at 425 MPa was destroyed during pressing.

Pressure [Tons]	Pressure [MPa]	Green body density [% of theoretical]
0.8	100	37.9
0.9	112	44.7
1.2	150	48.1
1.4	175	44.7
2.4	300	47.4
3.4	425	-

4.7 Results of sintering

Measured average densities for samples sintered at 1200 °C and 1300 °C for 4 hours in platinum crucibles are listed in Table 4.5. The samples sintered at 1200 °C had some dark brown spots in otherwise white samples. The samples sintered at 1300 °C or above had a uniformly brown color. After 14 days, the color of the BTO-n samples had changed from a uniform brown color to a camouflage-pattern of different shades of brown, shown in Figure 4.7. The BTO-a sample sintered at 1350 °C showed evidence of liquid phase formation.

Table 4.5: Average densities of sintered samples of the different synthesis routes, measured by the Archimedes' method. The densities are given as percentage of theoretical density for $BaTiO_3$, which is 6.02 g cm^{-3}. Deviation is given as one standard deviation.

Sample type	Sintering temperature [°C]	Average density [% of theoretical]
BTO-a	1200	-
	1300	93.8 ± 0.86
BTO-c	1200	57.3 ± 2.16
	1300	92.1 ± 0.79
BTO-n	1200	-
	1300	88.7 ± 3.55

Figure 4.7: Pictures of a sintered BTO-c sample (left) and sintered BTO-n sample (right) 14 days after sintering. Both samples were sintered at 1300 °C for 4 hours.

4.8 Piezoelectric properties

The measured piezoelectric properties of BTO-a, BTO-c, and BTO-n are presented in Table 4.6 and in Figure 4.8 - Figure 4.13. The polarization and displacement curves are averages of several samples, but the amount of samples from the different synthesis route varies. The piezoelectric coefficient and permittivity curves were only recorded for one sample from each synthesis route. This is due to the fact that the samples had a tendency to spark, or electrically discharge, during measurements. This happens due to porosity or highly conductive areas in the samples. The sparked samples will not give correct measurements and they were therefore discarded.

Table 4.6: Measured piezoelectric properties for BTO-a, BTO-c, and BTO-n samples. All samples are sintered at 1300 °C for 4 hours. P_r is remnant polarization, D_{max} is maximum displacement, d_{33} is the piezoelectric constant in the direction parallel to the polarization, and ε_r is the permittivity. Deviation is given as one standard deviation.

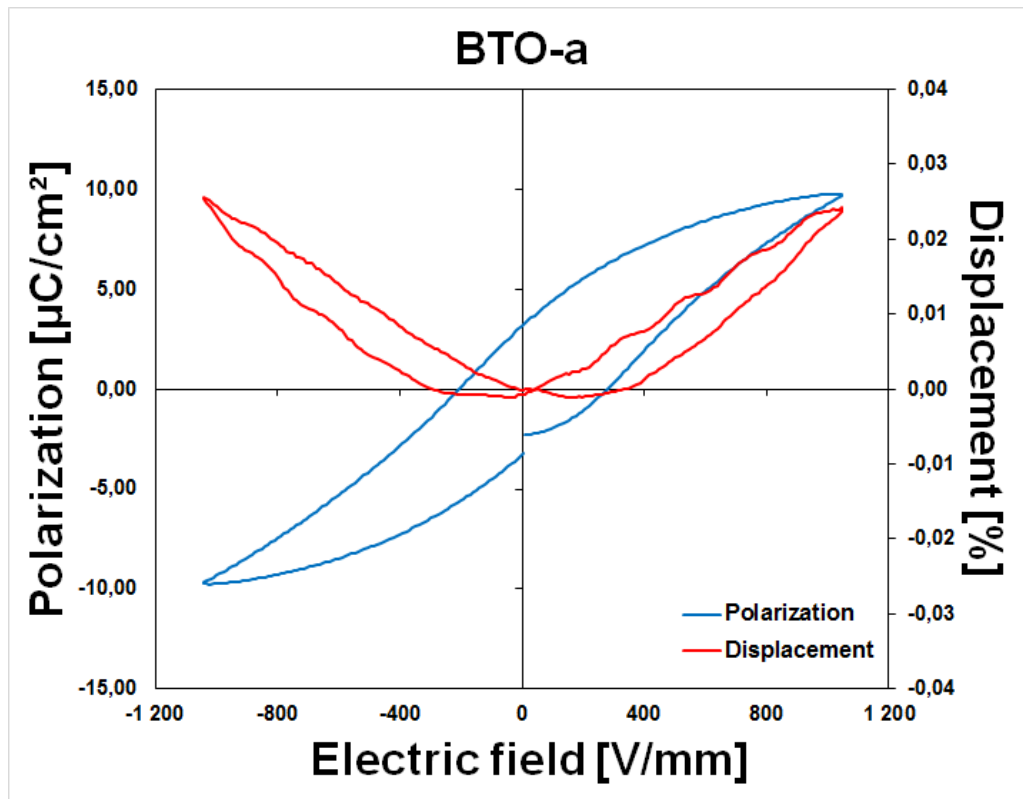| Sample type	Number of samples	P_r [μC cm^{-2}]	D_{max} [%]	d_{33} [nm V^{-1}]	ε_r [-]
BTO-a	1	3.27	0.026	0.05	2690
BTO-c	4	6.32 ± 0.97	0.033 ± 0.007	0.14	2700
BTO-n	2	9.30 ± 0.05	0.026 ± 0.001	0.11	2880

Figure 4.8: The polarization-electric field and displacement-electric field curves of the BTO-a sample, acquired at 1100 V mm^{-1} and 1 Hz.
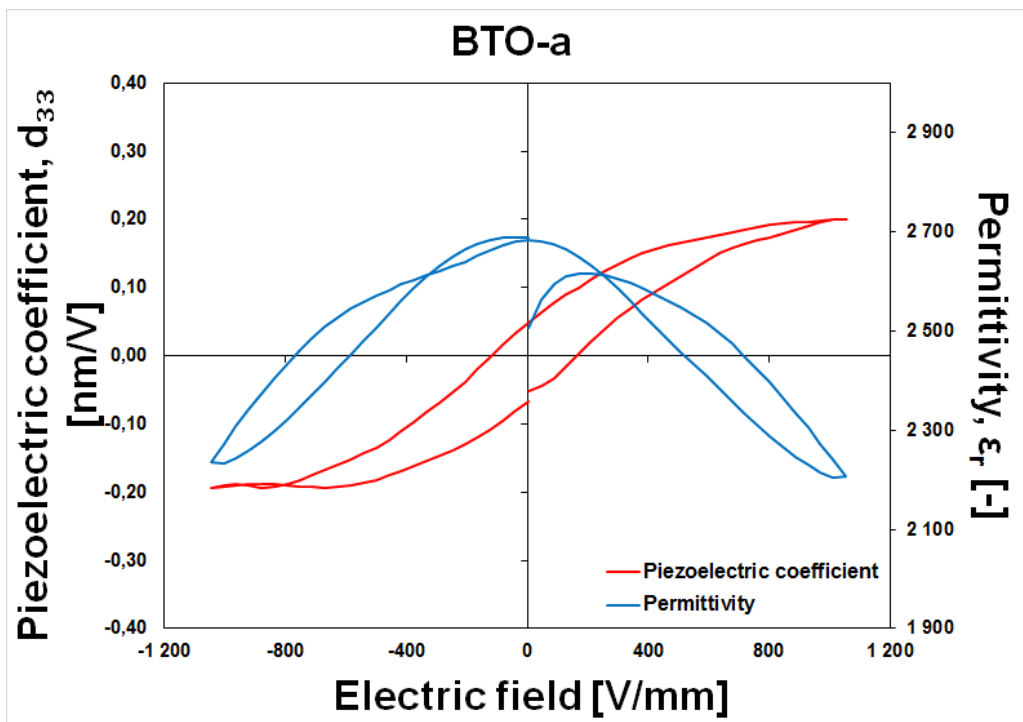

Figure 4.9: The piezoelectric coefficient-electric field and permittivity-electric field curves for BTO-a, acquired at 1100 V mm^{-1} and 1 Hz.
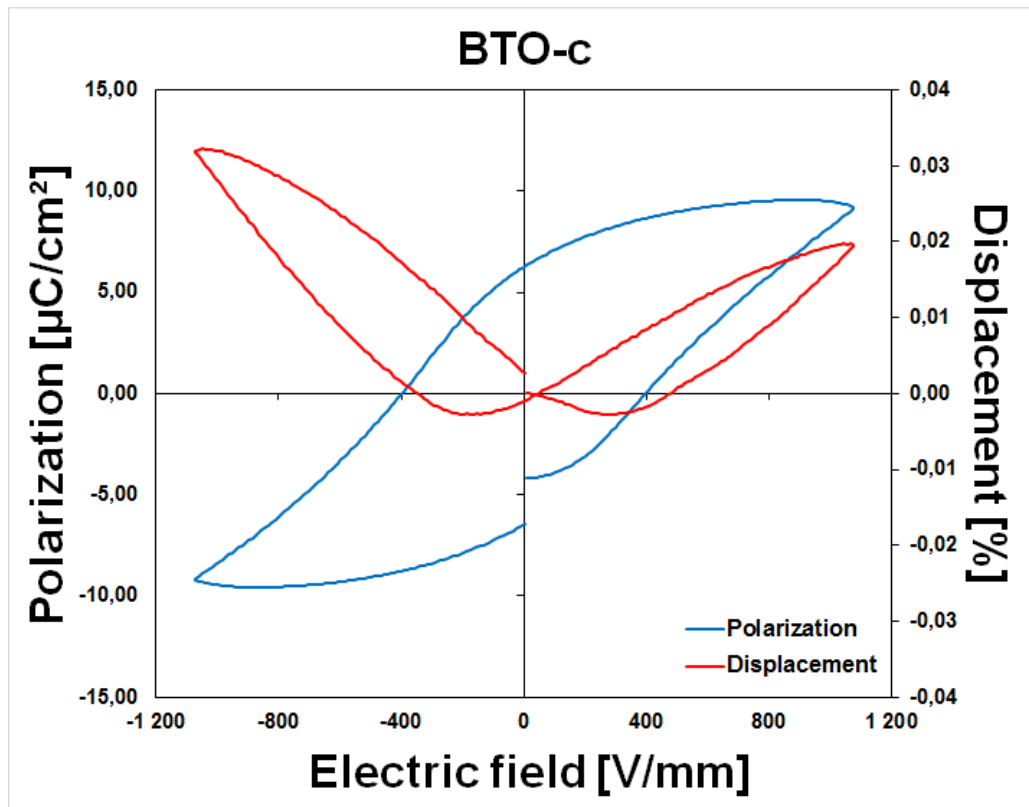
Figure 4.10: The polarization-electric field and displacement-electric field curves of BTO-c, acquired at 1100 V mm^{-1} and 1 Hz.
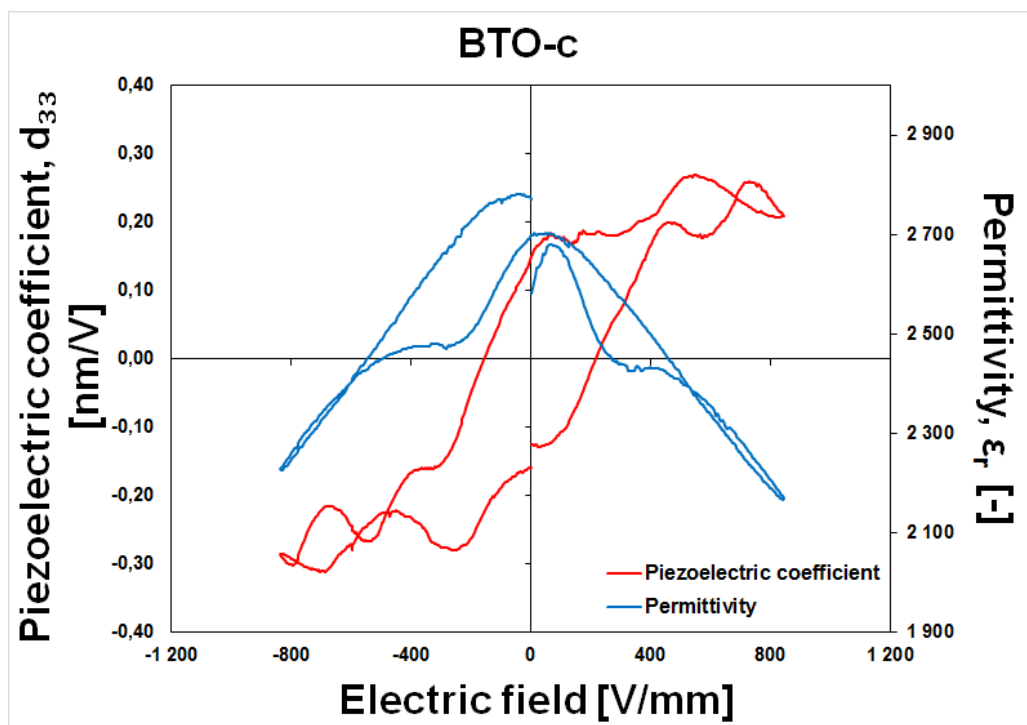

Figure 4.11: The piezoelectric coefficient-electric field and permittivity-electric field curves of BTO-c, acquired at 1100 V mm^{-1} and 1 Hz.
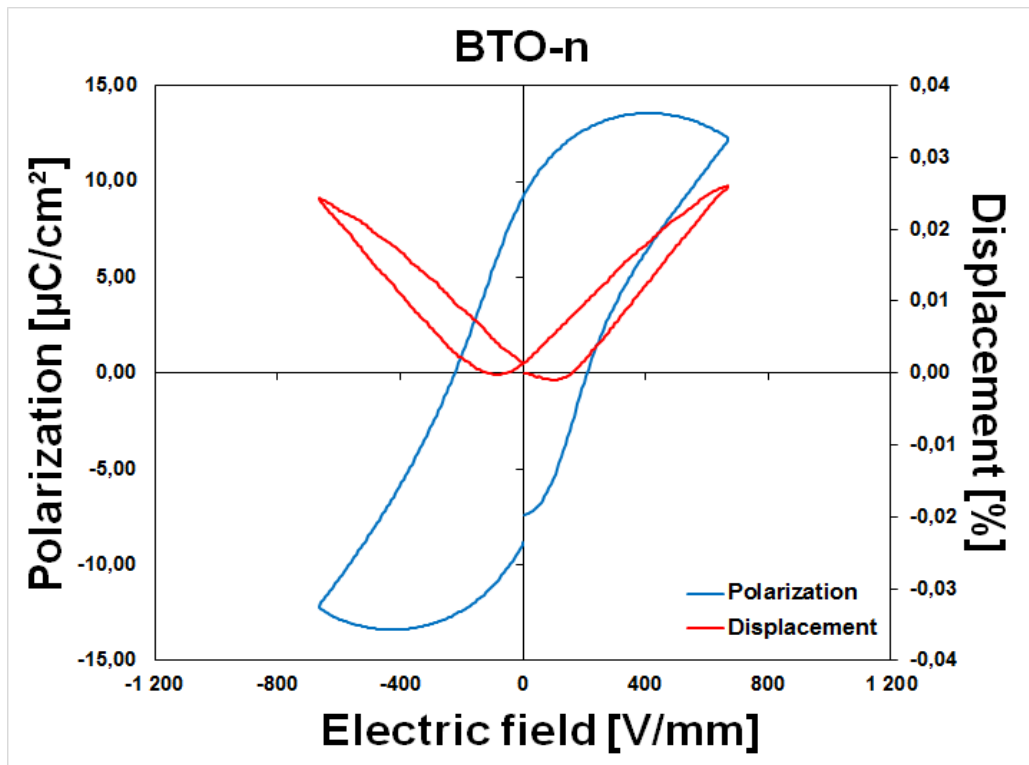
Figure 4.12: The polarization-electric field and displacement-electric field curves of BTO-n, acquired at 700 V mm^{-1} and 1 Hz. The low acquisition field is due to high tendency to discharge.
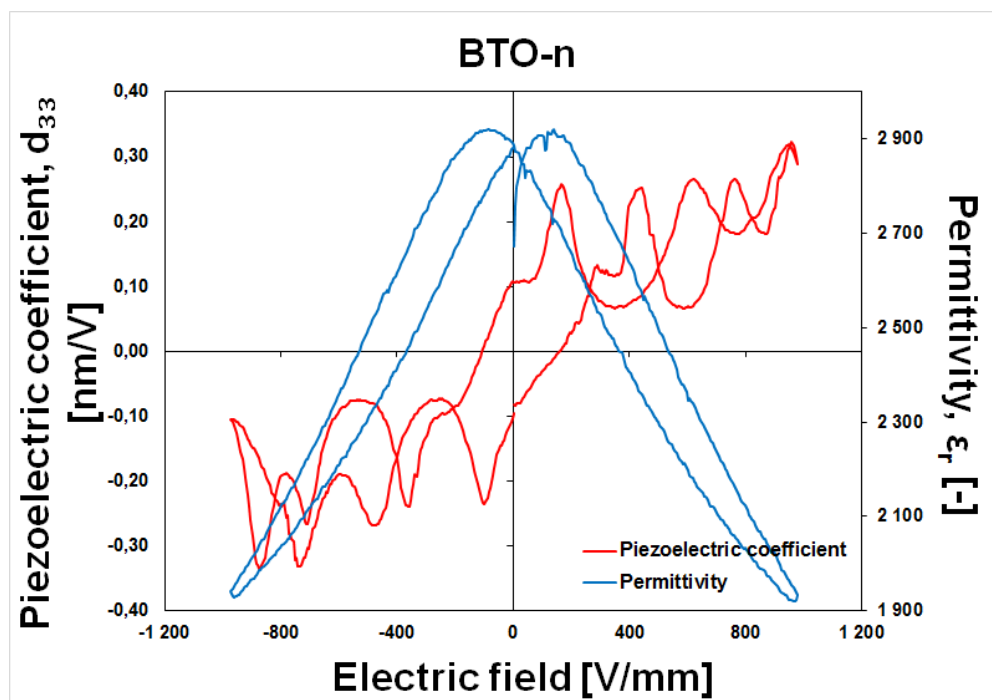

Figure 4.13: The piezoelectric coefficient-electric field and permittivity-electric field curves of BTO-n, acquired at 900 V mm^{-1} and 1 Hz.

4.9 SEM and EDS of sintered samples

4.9.1 BTO-c

SEM imaging of the BTO-c samples showed evidence of plate-like grains present in the material. This can be seen in the left image in Figure 4.14. The right image presents the sintered and etched sample investigated with EDS. The red line indicates where the analysis was done, starting inside a platelet and ending in the surrounding material. The result of the EDS scan is given in Figure 4.15. As can be seen from the figure, the plate-like structures (left side, 0-7 μm) contained approximately 42 wt. % Ba, 33 wt. % Ti, and 25 wt. % O. The surrounding material (right side, 7-14 μm) contained approximately 65 wt. % Ba, 25 wt. % Ti, and 20 wt. % O. The results for the plate-like structures corresponds to the element weight ratio in $BaTi_2O_5$ while the surrounding phase corresponds to $BaTiO_3$. 0.8 wt. % Al was also found in the BTO-c samples, but was not visible in the SEM images.
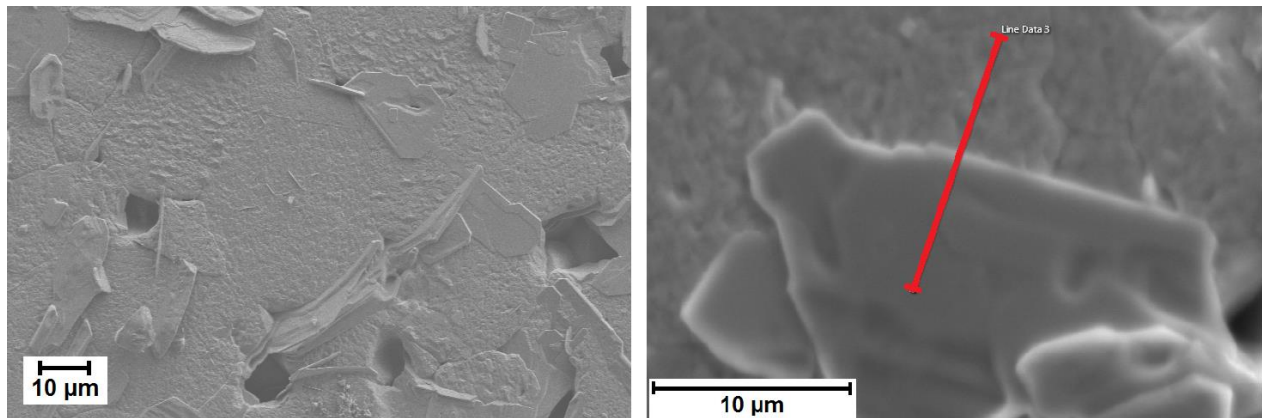

Figure 4.14: To the left is a SEM image of a BTO-c sample sintered at 1300 °C for 4 hours, polished, and then thermally etched at 1250 °C for 5 minutes. To the right is a SEM image of a BTO-c sample sintered at 1300 °C for 4 hours, polished, and then thermally etched at 1250 °C for 8 minutes.
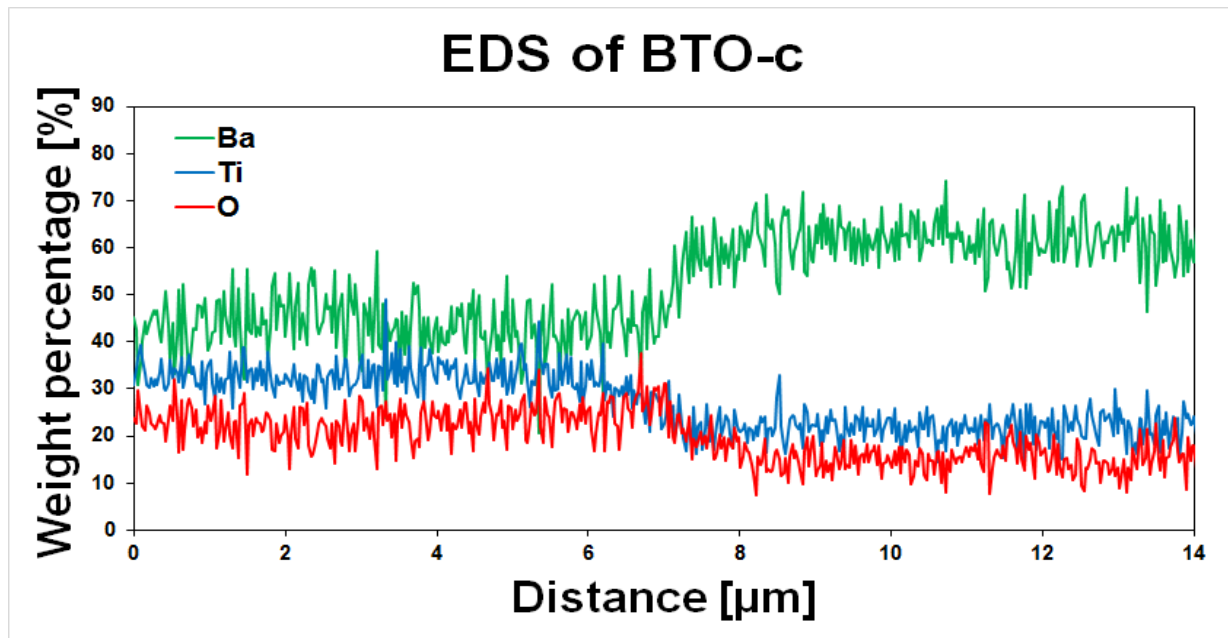
Figure 4.15: EDS of a BTO-c sample. The left side (distance 0-7 µm) shows the element distribution inside the plate-like structures in the samples. The right side (distance 7-14 µm) shows the element distribution in the material surrounding the plate-like grains.

4.9.2 BTO-n

SEM imaging of the BTO-n samples indicate that the color variation in the sample seen in Figure 4.7 is caused by variation in degree of porosity. The darker areas on the pellet appear to have higher density, as seen in Figure 4.16. The left and right image in Figure 4.16 shows the SEM image of BTO-n samples acquired with secondary electron and backscatter electron detectors respectively. The EDS results in Figure 4.17 indicate that there is no change in the weight percentage of the different elements in the sample. The element weight ratio of the entire sample corresponds to that of $BaTiO_3$. There is more variation in the weight percentage ratios in the left side of the curve, which is to be expected as it corresponds to the porous area of the sample. 0.3 wt. % Al was found in the BTO-n samples, but was not visible in the SEM images.

Figure 4.16: To the left is a SEM image of a BTO-n sample sintered at 1300 °C for 4 hours, polished, and then thermally etched at 1250 °C for 5 m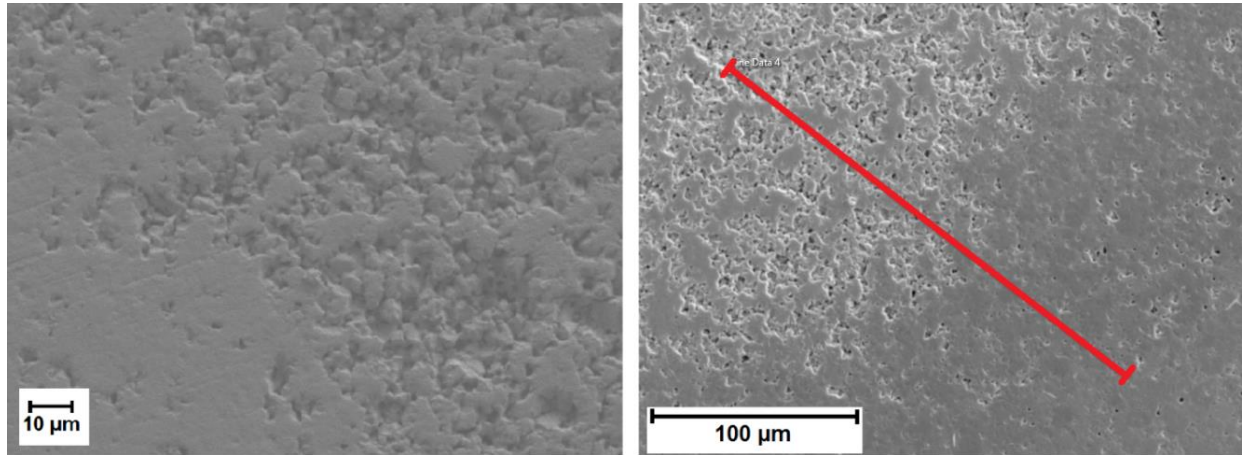inutes. To the right is a SEM image of a BTO-n sample sintered at 1300 °C for 4 hours, polished, and then thermally etched at 1250 °C for 8 minutes.
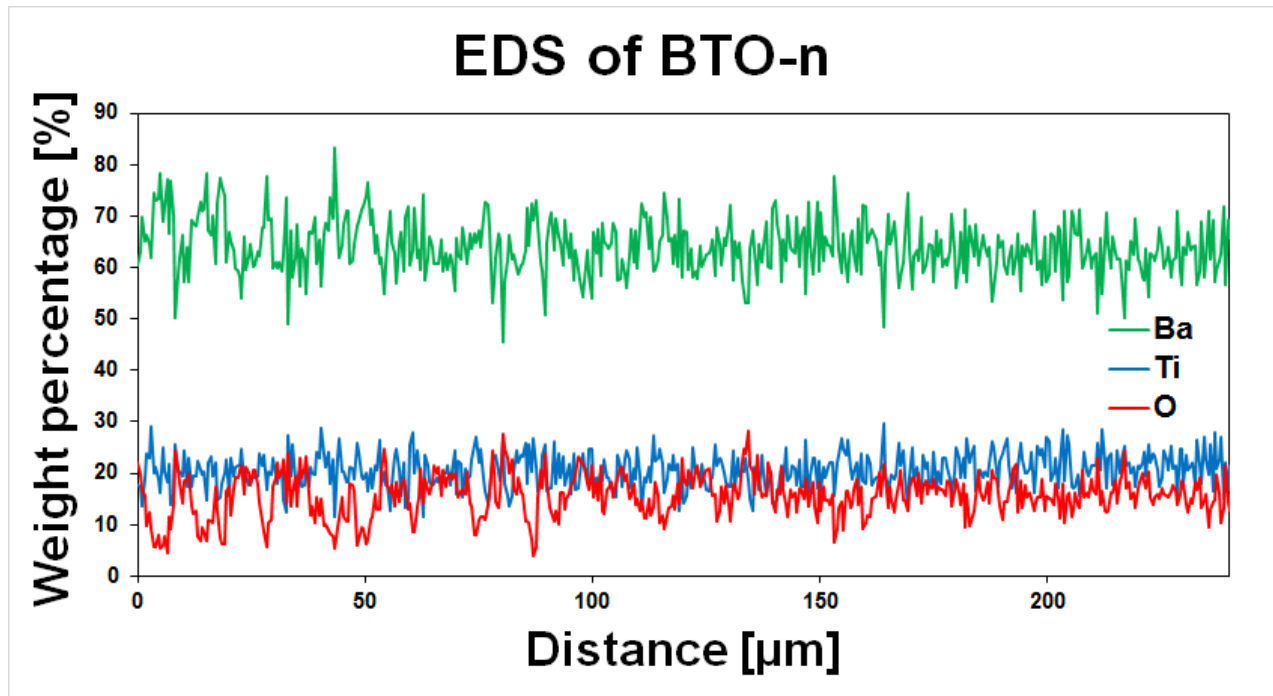

Figure 4.17: EDS of a BTO-n sample. To the left it is evident that the composition varies more that in the right area of the figure, due to the higher porosity.

4.10 Viscosimetry

The results of the viscosity testing can be seen in Table 4.7. Testing of viscosity was only done for one sample, as the viscosity was not expected to change much between samples with very similar composition, and because the suspensions of the complete systems were not stable. For the viscosity data to be relevant, the suspensions should be stable for at least 24 hours, so that viscosity is not changing during a spray pyrolysis process. The viscosity of BTO-c was compared to the viscosity of a commercial TiO_2-dispersion (Aerodisp w 740x, Evonik Industries, Germany). The results indicate that the BTO-c sample is much less viscous than the commercial sample.

Table 4.7: Results of viscosity measurements on Aerodisp w 740x dispersion and BTO-c suspension.

Sample	Viscosity [mPa s]
Aerodisp w 740x	3,758
BTO-c	1,519

5 Discussion

5.1 Suspension stability

The stabilities of the BTO-c and BTO-n suspensions were shown to be rather poor, as sedimentation occurred less than 20 minutes after preparation of the suspensions. This lead to a number of problems that are discussed further in the subsequent sections. Stable TiO_2 aqueous dispersions were however much easier to obtain. This is as expected as DLVO theory predicts that the more ions are present in a suspension, the higher the tendency to form agglomerates. Thus, obtaining stable dispersions of TiO_2 in water should be easier than obtaining stable suspensions of TiO_2 in solutions of barium nitrate as more ions are present in the barium nitrate solution.

The two dispersants tested in this work both decreased the rate of agglomeration. For the Dolapix A 88, this as can be seen from Figure 4.4. Here it is evident that for the samples containing Dolapix A 88 (Samples 3, 6, 9, 12, 15, and 18), the sedimentation layer is denser than for the samples without added dispersant. This means that the particles are packed closer together, implying smaller agglomerates. However, the stabilities of the samples were not good. In the samples containing Darvan C-N on the other hand, the sediment layer did not form at all during the first 24 hours. The dispersions were stable for several weeks. The concentration of TiO_2 in these samples did not seem influence the stability, so further testing would be needed to find the concentration limit of TiO_2.

Based on the results from the TiO_2 dispersion testing, the Darvan C-N was chosen for all further testing, to limit the number of variables. Only the Dolapix A 88 and the Darvan C-N were considered in this work, due to availability. A combination of both dispersants was not considered due to the already large number of variables in the stabilization tests.

For the BTO-n and BTO-c suspensions, stability was not obtained. However, the BTO-n samples seemed to have a higher tendency to form agglomerates, as seen from the height of the sedimentation layer in Figure 4.5. The layer was denser for BTO-c samples than for BTO-n, implying smaller particles. This again implies that less agglomeration has occured. This is as expected as the complexing agents in the BTO-c suspensions neutralize ionic charges, and decrease the driving forces for agglomeration.

Addition of $Ba(NO_3)_2$ to the dissolved EDTA (see section 3.1) should be done slowly, as the rate of the complexion reaction is dependent on kinetics. Failing to do this slow enough may have led to uncomplete complexion reactions in the BTO-c suspensions. This may again have led to barium precipitation, since $Ba(OH)_2$ may precipitate in aqueous solutions of $Ba(NO_3)_2$. Although no evident precipitation occurred in the barium solutions, this should be taken into account when making the precursor solutions.

The BTO-c suspensions showed the most promising results with regards to agglomeration, and in an attempt to increase the suspension stability, suspension samples of BTO-c with different amounts of dispersant were made, as seen in Figure 4.6. A slight increase in time before sedimentation begun was observed with increasing amount of dispersant, see Figure 5.1. This figure also shows an additional ultrasonic treatment after the mixing of the precursor dispersion and solution had a slight positive effect on sedimentation rate. This is seen by the larger height of the clear liquid border after 1 hour for samples 4 and 6 than for samples 3 and 5. As all these four samples end up with approximately the same sedimentation layer height after 24 hours, indicating that they have the same degree of agglomeration, even if the rate of agglomeration varies. The samples that were given the additional ultrasonic treatment use longer time before the sediment layer is fully formed, and this is an indication of slightly better stability. These trends are illustrated in Figure 5.1.

Zeta potential analysis of the precursor solutions and dispersions, and of the BTO-c and BTO-n suspensions, would give a better indication of what parameters increase suspension stability. E.g. by measuring zeta potential while adding dispersant, the optimal amount of dispersant could be found.
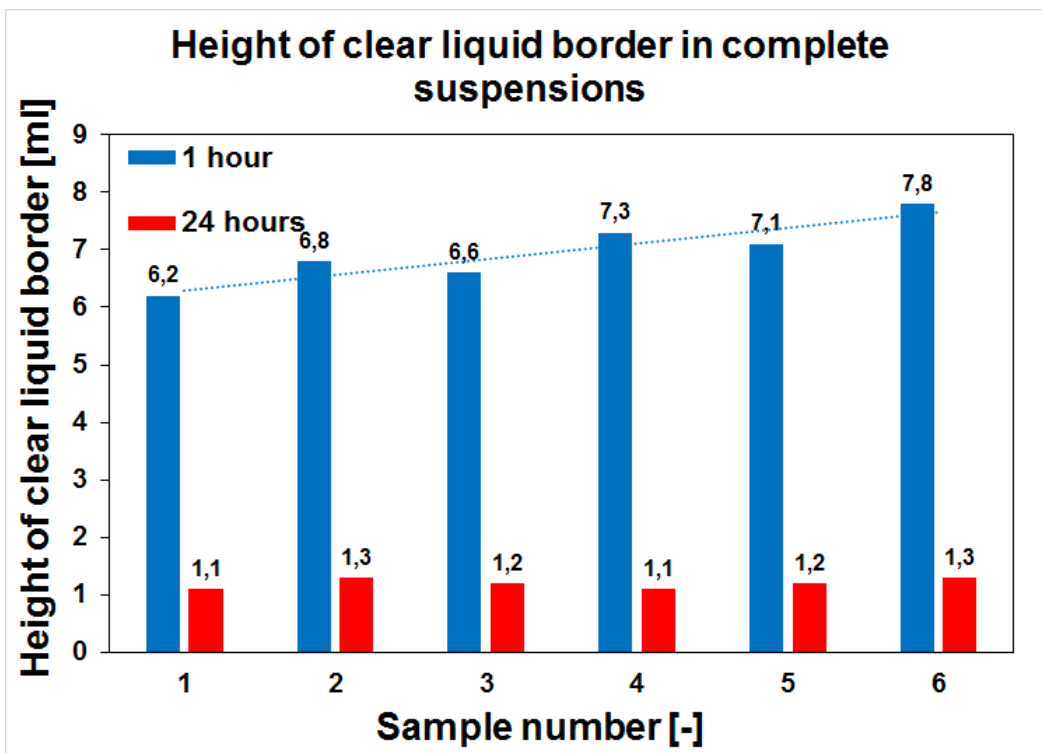
Figure 5.1: The slight increase in time before sedimentation can be seen as the height of the clear liquid border after one hour is increased with increasing amount of dispersant. The end sedimentation layer heights are not changed, implying that degree of agglomeration does not change. For sample explanations, see table 4.3.

5.2 Powder synthesis

The stabilities of the precursor suspensions are an important factor in the spray-pyrolysis process. Sedimentation while spraying may lead to loss of product, loss of stoichiometry control and formation of secondary phases. The powders calcined at 800 °C did not show any indication of secondary phase formation or contamination, except for the BTO-n powders. XRD of the calcined powder suggested formation of the Ba_2TiO_4-phase, although no later analysis could confirm this.

The SEM images of the BTO-c as synthesized powder, as seen in Appendix B, indicates that $BaCO_3$ precipitates on the surface of the TiO_2 particles during the spray pyrolysis. This is favorable in regards to obtaining small particle size and in the subsequent heat treatments in regards to reactions between TiO_2 and $BaCO_3$ to form $BaTiO_3$.

The spray pyrolysis process did not lead to complete reactions between the precursors to form phase-pure $BaTiO_3$. Calcination was therefore necessary to complete the reaction. Having the precursors react fully during spraying would be favorable due to the lower energy cost of avoiding subsequent heat treatment. However, due to the short residence time of particles in the spray-pyrolysis furnace, this is not likely to be obtainable.

As mentioned in section 4.1, some product was lost during the spraying. The main reason for this is believed to be sedimentation of the suspensions during spraying. This indicates that stirring the suspensions during spraying is not sufficient, and suspension stability should be increased.

5.3 Sintering behavior

The color change of the samples when sintered at 1300 °C was an indication that secondary phases or some contamination was present in the powders. This is discussed in more detail in section 5.4.

Sintering at 1200 °C yielded low densities. As the results in table Table 4.5 shows, the density of the BTO-c samples averaged at around 57 %. This value increased significantly (to 92 %) when sintering temperatures were increased to to 1300 °C. This was the maximum possible sintering temperature, due to indications of liquid phase formation when sintering at higher temperatures. This was as expected from the phase diagram seen in Figure 2.6. To increase density, longer sintering times at max. temperature could be investigated, but this might promote grain growth instead of densification.

The crucible material did not seem to affect the results in any way, but platinum crucibles were used for the samples that were made for piezoelectric testing, SEM, and EDS to eliminate crucible material as a source of contamination.

5.4 Secondary phase formation and contamination

The presence of a secondary phase or contamination became clear after sintering. Pure $BaTiO_3$ has a white color, and the samples produced in this work all had brown/grey color. The color was more evident in denser samples, and as seen in Figure 4.7 and discussed in section 4.7, it is evident that denser areas have a darker brown color. This suggests that some form of contamination that causes the discoloration is present in the $BaTiO_3$ matrix. The color is more prominent in the BTO-c samples than in BTO-n samples. This contamination may come from trace amounts of aluminum, as discussed in section 4.9. This is further backed by work done by Astri Bjørnetun Haugen on sintering of calcium-doped barium titanate, where similar powders from CerPoTech AS were shown to contain this kind of contamination.[43]

The difference in degree of discoloration could be explained by the fact that more aluminum was present in the BTO-c samples, as discussed in section 4.9. This may be due to the secondary phase which was present in the BTO-c samples, as seen in Figure 4.15. It is believed to be $BaTi_2O_5$. The contamination leading to the discoloration may be more soluble in this phase, thus leading to a darker color than in the BTO-n samples. The secondary $BaTi_2O_5$ phase most likely originates from loss of stoichiometry control due to sedimentation during the spray-pyrolysis process.

The source of the aluminum contamination was not confirmed, but the TiO_2-nanopowder could contain some Al_2O_3. The datasheet for the TiO_2[41] used in this work does not

mention aluminum content, but similar TiO_2 products to the powder used in this work has been reported to contain up to 0.3 wt. % Al_2O_3.[44] This would however not explain the presence of the contamination in the BTO-a samples. The BTO-a samples were produced with titanium isopropoxide, not TiO_2. The factors that are identical for all synthesis routes and that might be a source of aluminum contamination are the $Ba(NO_3)_2$ precursor, the spray-pyrolysis process, and the calcination in Al_2O_3 crucibles. The $Ba(NO_3)_2$ datasheet gives no information about aluminum content.[40]

The formation of the camouflage-like pattern in the BTO-n samples over time has not been explained, but appears to be some kind of mass diffusion over time, as the samples became denser in some areas and more porous in others. The larger variation in density in the BTO-n samples compared to the BTO-c samples can also be seen from the standard deviation from the average density in Table 4.5.

5.5 Piezoelectric properties

Testing the piezoelectric properties was difficult because of the high tendency the samples had to experience electrical discharge. This discharge, or sparking, may be related to the porosity of the samples. The air in the pores has a lower dielectric breakdown strength than the surrounding $BaTiO_3$. This allows for easier charge migration through the sample, leading to a short-circuit during testing. This hypothesis is backed by the fact that the BTO-n samples, which had lower density than the BTO-c samples, had a tendency to spark more easily.

The measured values for BTO-a, BTO-c and BTO-n seen in Table 4.6 are comparable to values found in literature with regards to polarization, piezoelectric coefficient, and permittivity.[3][2] The displacement is however much lower. The reason for this is not known. Additionally, it is difficult to say how the detected contamination affects the piezoelectric properties.

However, in Figure 4.11, the permittivity curve for the BTO-c sample can be seen to have both primary and secondary peaks for both negative and positive field. This is accentuated in Figure 5.2, where A is the primary peak for positive field, B is the secondary peak for positive field, C is the primary peak for negative field and D is the secondary peak for negative field. This phenomenon is discussed by Bar-Chaim et al.[45] and is related to the independent switching of ferroelectric domains with different orientations, and the effect this has on permittivity. A 180° switch in polarization direction happens at weaker fields than s 90° switch. This is again related to the extra strain induced in the material when domains do a 90° switch as compared to a 180° switch. This phenomenon does not occur in the BTO-a and BTO-n samples (Figure 4.9 and Figure 4.13), where the permittivity curve is smooth, and does not have the secondary peaks. This implies that in the BTO-c sample, the ferroelectric domains have a larger variety of orientation prior to polarization than in the BTO-a and BTO-n samples, and the BTO-a and BTO-n samples might possibly have predominantly 0 and 180 ° oriented ferroelectric domains. This may be the reason for the larger maximum displacement in

the BTO-c samples seen in Table 4.6, as the 90 ° switching of domains induces more strain in the material. This effect can also be seen in the displacement of BTO-c in Figure 4.10, by the larger change in the displacement curve at low electric field than in Figure 4.8 and Figure 4.12 for BTO-a and BTO-n respectively
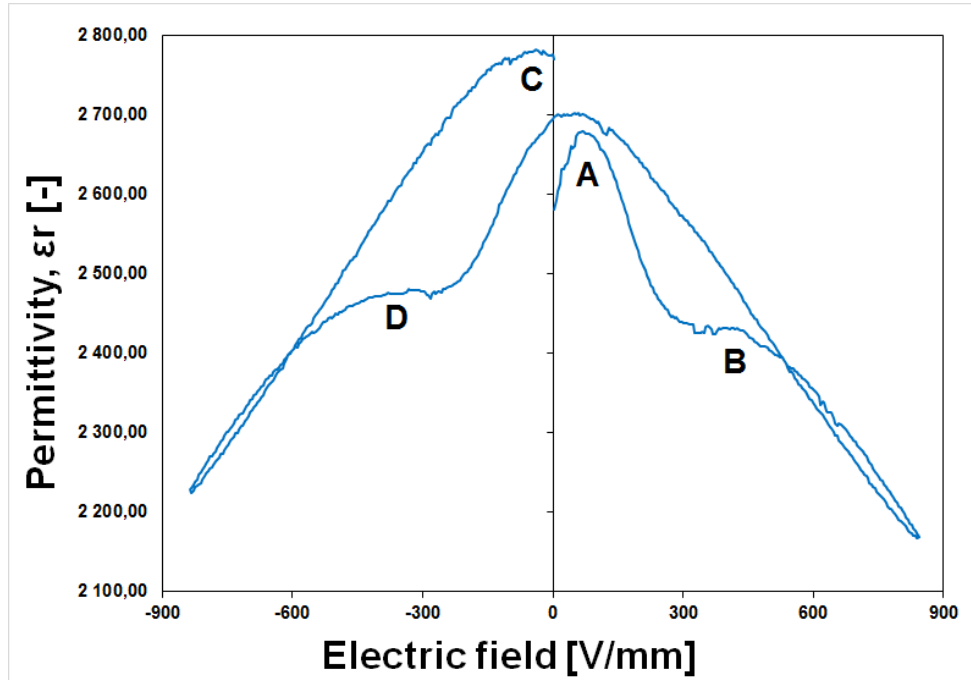

Figure 5.2: Primary and secondary peaks in permittivity for BTO-c in positive (A and B) and negative (C and D) electric field. The primary peaks represent the 180° switching of ferroelectric domains whereas the secondary peaks represent the 90° switching of ferroelectric domains.

6 Concluding remarks and further work

A novel synthesis method for production of $BaTiO_3$-nanoparticles has been investigated. The method consists of spray-pyrolysis of suspensions of TiO_2-nanoparticles in barium nitrate solutions, and different compositions and parameters have been investigated in regards to the properties of the produced powders.

It has been shown that the stabilities of the suspensions heavily influence the properties of the produced powder. Loss of stoichiometry due to sedimentation is a problem that needs to be addressed for the synthesis method to be used commercially. The effect of complexation of the barium ions in the precursor solutions was investigated, and results indicate that complexation may be necessary to obtain satisfactory suspension stability.

The piezoelectric properties of sintered pellets of the produced powders were analyzed. The values are comparable to values reported for $BaTiO_3$ in literature. Measurements of the permittivity in the samples indicate that complexation of the barium ions in the precursor suspensions may lead to a more random distribution of the ferroelectric domain orientations in the sintered samples. This effect is not seen for samples produced from solutions of titanium isopropoxide and barium nitrate.

Further work is needed to decide the applicability of this method. Zeta potential measurements during the preparation of the suspensions might aid in obtaining stable suspensions. Longer sintering times and more advanced sintering programs could be investigated to achieve higher density of the sintered samples.

Appendices

A. Calcination programs

Different calcination programs were investigated for the powder produced from the spray pyrolysis. The calcination programs that were used are shown in Table A.1. The time, heating rate and cooling rate were chosen based on standard calcination programs used by CerPoTech AS.

Table A.1: Calcination programs investigated for the produced powder.

Powder type	T_{max} [°C]	Time at T_{max} [h]	Heating rate [°C h^{-1}]	Total time [h]	Weight loss [%]
	600	6	200	12	6.7
BTO-a	700	6	200	13	7.2
	800	6	200	14	9.9
	600	6	200	12	11.2
BTO-c	700	6	200	13	13.1
	800	6	200	14	15.3
	600	6	200	12	32.0
BTO-n	700	6	200	13	32.3
	800	6	200	14	36.6

A significant weight loss in the samples during calcination was observed. As expected, there is a trend that increased calcining temperature increases weight loss, as more precursors react to $BaTiO_3$. The grey as synthesized powder of BTO-a and BTO-c turned white, also indicating the formation of $BaTiO_3$. The BTO-n powder had the largest weight loss. This is likely due to the reaction between $Ba(NO_3)_2$ and TiO_2 to $BaTiO_3$, seen in the x-ray diffractogram in Figure A.1. In the BTO-a and BTO-c powders, seen in Figures A.2 and A.3 respectively, $BaCO_3$ was produced during the spray-pyrolysis. This then reacted with TiO_2 to form $BaTiO_3$ during the subsequent calcination.
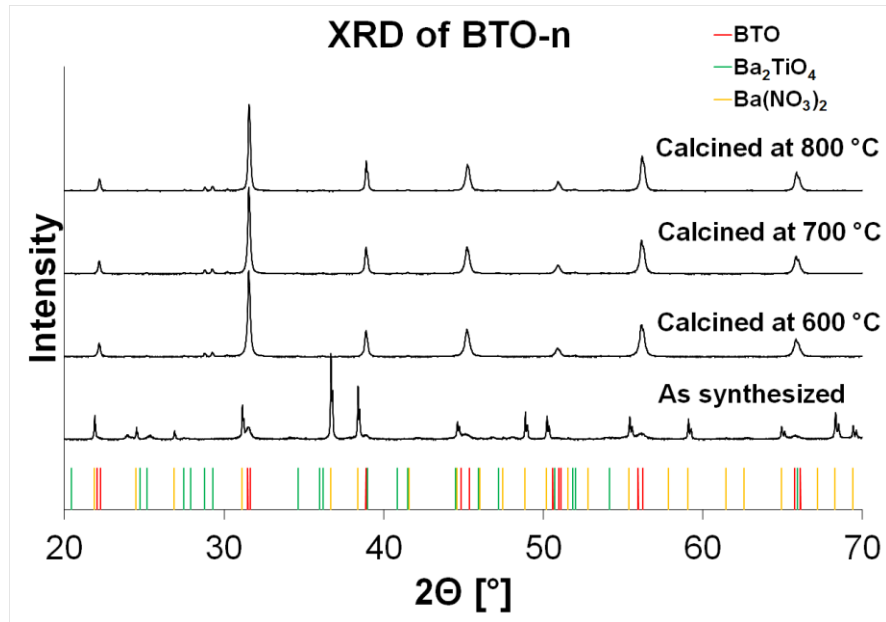
Figure A.1: XRD-diagram of resulting powder from the BTO-n synthesis route. All samples were calcined at the given temperatures for 6 hours. After calcination, almost phase-pure $BaTiO_3$ was achieved independent of calcination program, but small amounts of a secondary phase, believed to be Ba_2TiO_4, was present.[1]
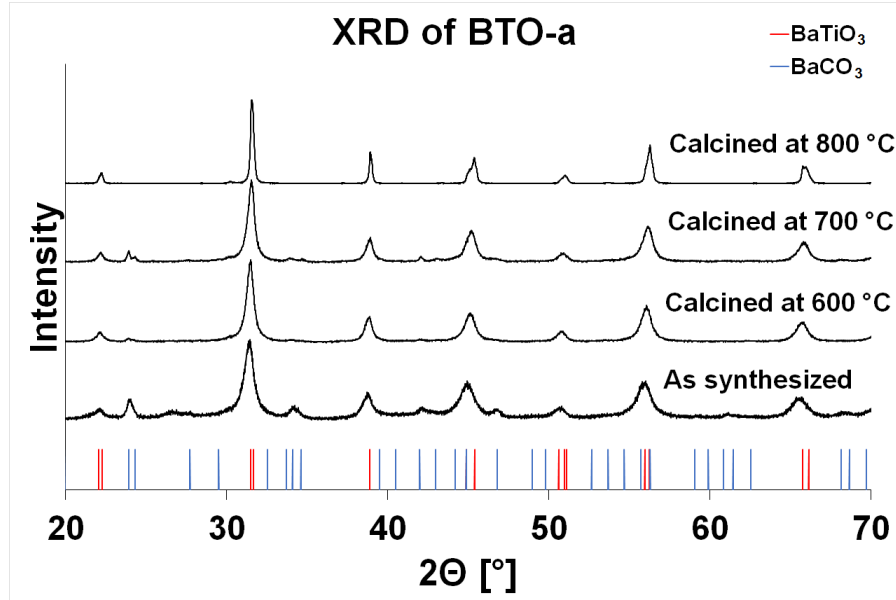

Figure A.2: XRD-diagram of resulting powder from the BTO-a synthesis route. All samples were calcined at the given temperature for 6 hours. It is evident from the diagram that BaCO3 was formed in the spray pyrolysis process and was present in the as synthesized powder. This phase burned off completely when calcining at 800 °C for 6 hours.[1]
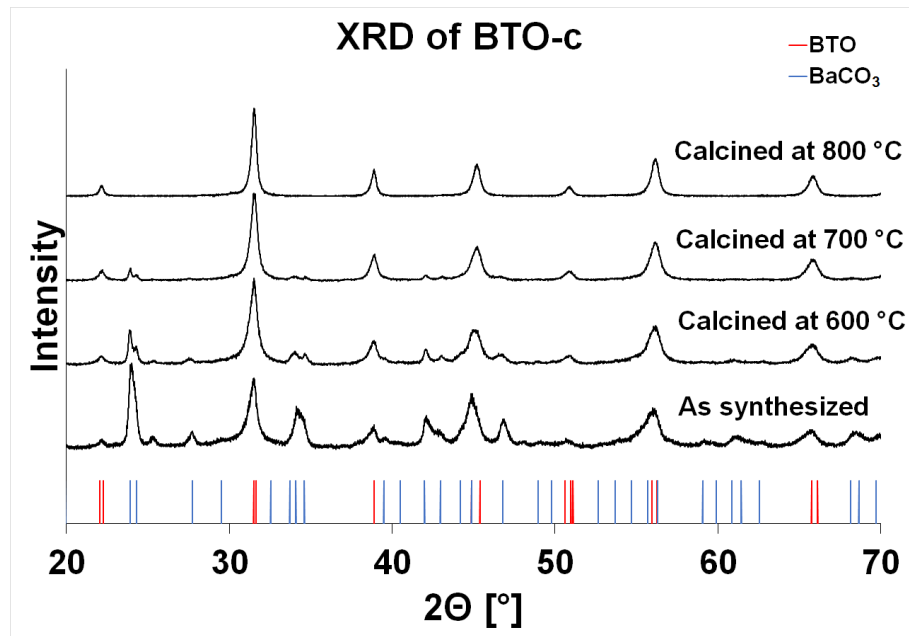
Figure A.3: XRD-diagram of resulting powder from the BTO-c synthesis route. All samples were calcined at the given temperature for 6 hours. $BaCO_3$ was formed in the spray pyrolysis process. This phase disappeared after calcining at 800 °C for 6 hours. The small, unmarked peaks in the as synthesized pattern stems from residual TiO_2.[1]

B. SEM imaging of as synthesized BTO-n and BTO-c powders

The as synthesized powders from the BTO-n and BTO-c synthesis routes are shown in Figure B.1. In the BTO-n powder, large agglomerates and porous particles dominated. Some large particles that appear to be solid can be seen in the lower left corner of Figure B.1 (A). These may be $Ba(NO_3)_2$ that has not reacted.

In the BTO-c powder, large agglomerates, porous particles and hollow shells dominate. Some smaller particles with rough surfaces are also present, see B.1 (B). This is believed to be precipitated $BaCO_3$ on the surface of TiO_2-particles.
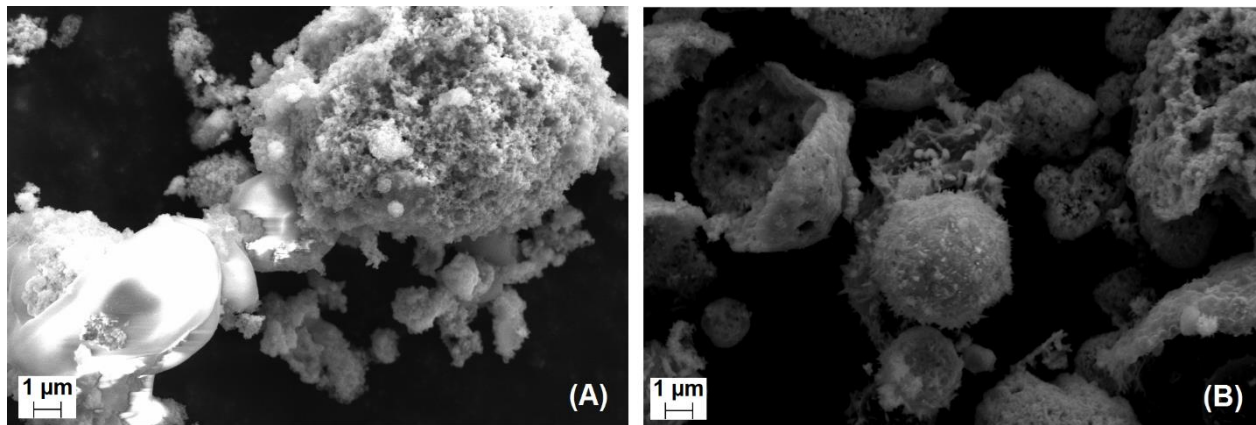

Figure B.1: As synthesized powder from the BTO-n (A), and BTO-c (B) synthesis routes.[1]

C. TGA of BTO-c powder

The as synthesized BTO-c powder was characterized by TGA (Thermogravimetric analysis) (STA449 jupiter, NETZSCH, Germany). The powder was heated with a heating rate of 200 °C h^{-1} to 800 °C and then held at constant temperature for 1 hour. The sample was then heated with a heating rate of 600 °C h^{-1} to 1200 °C and held for 2 hours at constant temperature before cooling at -600 °C h^{-1}. The temperature program and resulting mass loss can be seen in Figure C.1.
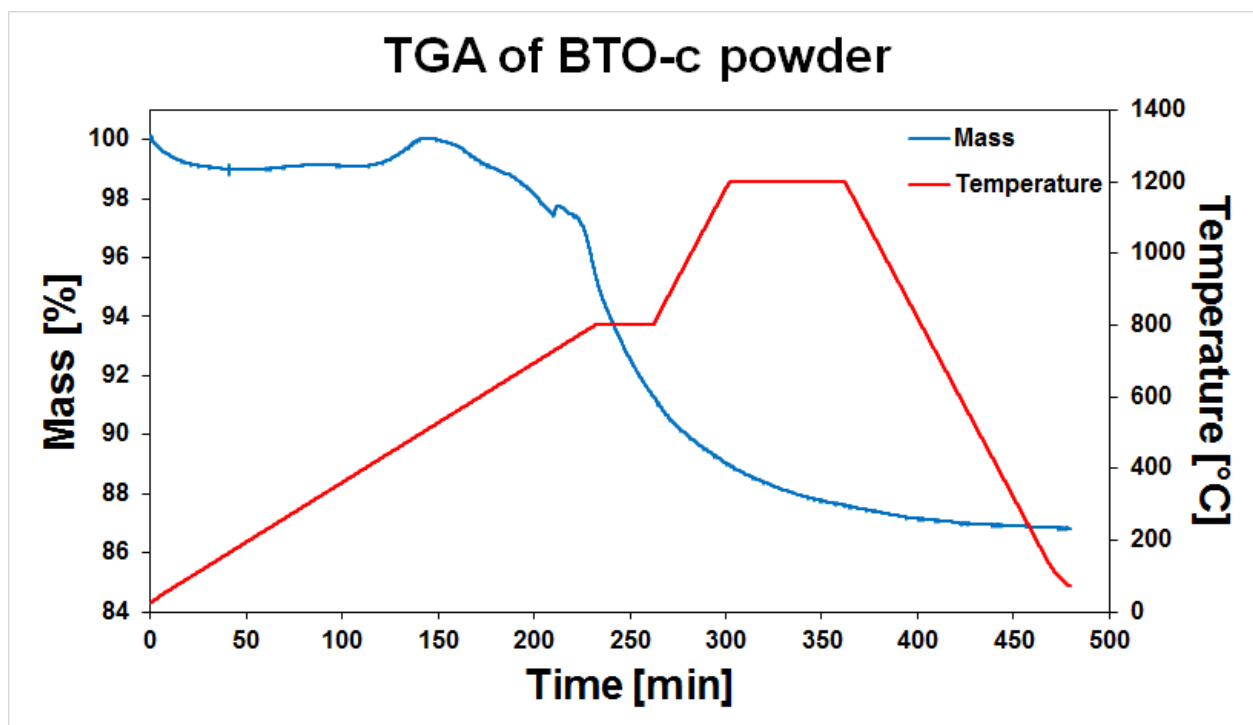

Figure C.1: TGA of the BTO-c as synthesized powder, with total mass on left axis, and temperature on right axis.

The main component of the mass loss begins at 800 °C and consists mainly of the burning of the organic complexing agents still present after the spray pyrolysis. The total mass loss is 14 %, which is similar to the mass loss after calcination seen in Table A.1. This means that little mass loss is expected during sintering as almost all organic compounds burn off during calcination.

Bibliography

1.   Gryteselv, M. A novel synthesis method for $BaTiO_3$-nanoparticles. Specialization project, Norwegian University of Science and Technology, 2015.
2.   Ertuğ, B., The Overview of The Electrical Properties of Barium Titanate. *American Journal of Engineering Research* **2013,** *2* (8).
3.   Shieh, J.; Yeh, J. H.; Shu, Y. C.; Yen, J. H., Hysteresis behaviors of barium titanate single crystals based on the operation of multiple 90° switching systems. *Materials Science and Engineering: B* **2009,** *161* (1–3), 50-54.
4.   Richerson, D. W., *Modern Ceramic Engineering*. Third edition ed.; CRC press: 2006.
5.   Haertling, G. H., Ferroelectric Ceramics: History and Technology. *Journal of the American Ceramic Society* **1999,** *82* (4), 797-818.
6.   Directive 2002/95/EC of the European Parliament and of the Council on the restriction of the use of certain hazardous substances in electrical and electronic equipment. union, T. E. p. a. t. c. o. t. E., Ed. 2003.
7.   Jaffe, B.; Cook, W. R.; Jaffe, H., *Piezolectric ceramics*. Academic Press: 1971.
8.   Singh, B. R.; Vatansever, D.; Siores, E.; Shah, T., *Global warming: Impacts and future perspective*. InTech: 2012.
9.   Myers, H. P., *Introductory solid state physics*. 2nd ed. ed.; London: Taylor and Francis: 1997.
10.   PICeramic Piezo technology. http://www.piceramic.com/piezo-technology/fundamentals.html (accessed 06.12).
11.   Perovskite structure. https://commons.wikimedia.org/wiki/File:Perovskite.svg (accessed 10. october).
12.   PiezoTechnologies. An Overview of the Properties of Different Piezoceramic Materials 2015. http://www.piezotechnologies.com/knowledge-desk/overview-piezo-materials.
13.   PiezoTechnologies, Usage Temperatures of Piezoceramic Materials. **2015**.
14.   Saito, Y.; Takao, H.; Tani, T.; Nonoyama, T.; Takatori, K.; Homma, T.; Nagaya, T.; Nakamura, M., Lead-free piezoceramics. *Nature* **2004,** *432* (7013), 84-87.

15.   Wang, J. J.; Wu, P. P.; Ma, X. Q.; Chen, L. Q., Temperature-pressure phase diagram and ferroelectric properties of BaTiO3 single crystal based on a modified Landau potential. *J. Appl. Phys.* **2010,** *108* (11), 8.

16.   Fu, D.; Itoh, M. Role of Ca off-Centering in Tuning Ferroelectric Phase Transitions in Ba(Zr,Ti)O3System, Ferroelectric Materials - Synthesis and Characterization 2015. http://www.intechopen.com/books/ferroelectric-materials-synthesis-and-characterization/role-of-ca-off-centering-in-tuning-ferroelectric-phase-transitions-in-ba-zr-ti-o3system.

17.   CerPoTech Targets. http://www.cerpotech.com/target (accessed 08.12).

18.   Lee, S.; Randall, C. A.; Liu, Z.-K., Modified Phase Diagram for the Barium Oxide–Titanium Dioxide System for the Ferroelectric Barium Titanate. *Journal of the American Ceramic Society* **2007,** *90* (8), 2589.

19.   Derjaguin, B.; Landau, L., Theory of the stability of strongly charged lyophobic sols and of the adhesion of strongly charged particles in solutions of electrolytes. *Progress in Surface Science* **1993,** *43* (1), 30-59.

20.   Zeta potential: a complete course in 5 minutes. http://www.zeta-meter.com/5min.pdf (accessed 23.05).

21.   Trefalt, G.; Borkovec, M. Overview of DLVO theory 2014. http://www.colloid.ch/grouppage/pdfs/Overview_DLVO_Theory1.pdf (accessed 23.05).

22.   Fasaki, I.; Siamos, K.; Arin, M.; Lommens, P.; Van Driessche, I.; Hopkins, S. C.; Glowacki, B. A.; Arabatzis, I., Ultrasound assisted preparation of stable water-based nanocrystalline TiO2 suspensions for photocatalytic applications of inkjet-printed films. *Applied Catalysis A: General* **2012,** *411–412*, 60-69.

23.   Yaremko, Z. M.; Tkachenko, N. H.; Bellmann, C.; Pich, A., Redispergation of TiO2 particles in aqueous solutions. *Journal of Colloid and Interface Science* **2006,** *296* (2), 565-571.

24.   Preocanin, T.; Kallay, N., Point of Zero Charge and Surface Charge Density of TiO_2 in Aqueous Electrolyte Solution as Obtained by Potentiometric Mass Titration. *Croatica Chemica Acta* **2006,** *79* (1), 95-106.

25.   Berger-Keller, N.; Bertrand, G.; Filiatre, C.; Meunier, C.; Coddet, C., Microstructure of plasma-sprayed titania coatings deposited from spray-dried powder. *Surface and Coatings Technology* **2003,** *168* (2–3), 281-290.

26.   Atkins, P.; Overton, T.; Rourke, J.; Weller, M.; Armstrong, F., *Inorganic Chemistry*. 4 th ed.; Oxford univeristy press: 2006.

27.   Ringbom, A., *Complexation in Analytical Chemistry*. Interscience Publishers: 1963; Vol. 16.

28.   Capitaneo, J. L.; Caffarena, V. d. R.; Ogasawara, T.; Pinho, M. S. Performance of radar absorbing nanocomposites by waveguide measurements 2008, p. 319-324. http://www.scielo.br/scielo.php?script=sci_arttext&pid=S1516-14392008000300015&lng=en&nrm=iso.

29.   https://commons.wikimedia.org/wiki/File:Medta.png (accessed 18.06).

30.   Messing, G. L.; Zhang, S.-C.; Jayanthi, G. V., Ceramic Powder Synthesis by Spray Pyrolysis. *Journal of the American Ceramic Society* **1993,** *76* (11), 2707-2726.

31.   CerPoTech Spray Pyrolysis. http://cerpotech.com/spraypyrolysis (accessed 08.12).

32. Patterson, A. L., The Scherrer Formula for X-Ray Particle Size Determination. *Physical Review* **1939,** *56* (10), 978-982.
33. Langford, J. I.; Wilson, A. J. C., SCHERRER AFTER 60 YEARS - SURVEY AND SOME NEW RESULTS IN DETERMINATION OF CRYSTALLITE SIZE. *J. Appl. Crystallogr.* **1978,** *11* (APR), 102-113.
34. Speaksman, S. A. Esimating crystallite size using XRD. prism.mit.edu/xray/oldsite/CrystalSizeAnalysis.ppt (accessed 08.12).
35. Kopeliovich, D. D. Methods of shape forming ceramic powders 2012. http://www.substech.com/dokuwiki/doku.php?id=methods_of_shape_forming_ceramic_powders (accessed 10.06.2016).
36. Riviera, T. Synthesis and Thermoluminescent Characterization of Ceramics Materials 2011. http://www.intechopen.com/books/advances-in-ceramics-synthesis-and-characterization-processing-and-specific-applications/synthesis-and-thermoluminescent-characterization-of-ceramics-materials (accessed 10.06.2016).
37. Buscaglia, M. T.; Bassoli, M.; Buscaglia, V., Solid-state synthesis of ultrafine BaTiO3 powders from nanocrystalline BaCO3 and TiO2. *Journal of the American Ceramic Society* **2005,** *88* (9), 2374-2379.
38. Zhao, X.; Liu, W. F.; Chen, W.; Li, S. T., Preparation and properties of BaTiO3 ceramics from the fine ceramic powder. *Ceram. Int.* **2015,** *41*, S111-S116.
39. Roh, Y. A.; Bin Humayoun, U.; Song, Y. H.; Kakihana, M.; Masaki, T.; Yoon, D. H., Influence of TiO2 precursors on BaTiO3 by liquid phase precursor method. *Ceram. Int.* **2015,** *41* (10), 12751-12756.
40. Product specification for barium nitrate. Alfa Aesar: www.alfa.com, 2016.
41. Product information of Titanium(IV) oxide, anatase-nanopowder. Sigma Aldrich: www.sigmaaldrich.com.
42. Sletnes, M. Wet chemical synthesis of silicon nanoparticles and phosphorescent oxides for white light emitting diodes Ph.D, Norwegian University of Science and Technology, 2014.
43. Haugen, A. B., Comparing BCT-batches. NTNU: 2016.
44. AEROXIDE TiO2 P25 product information. Evonik Industries: www.aerosil.com, 2016.
45. Bar-Chaim, N.; Brunstein, M.; Grünberg, J.; Seidman, A., Electric field dependence of the dielectric constant of PZT ferroelectric ceramics. *J. Appl. Phys.* **1974,** *45* (2398).